TU Delft

Delft University of Technology

Influence of constituent material on behavior of auxetic cellular composites

Zhang, Hongzhi; Song, Shuai; Jiang, Nengdong; Feng, Yujie; Qin, Jin; Ge, Zhi; Šavija, Branko

DOI
10.1016/j.jobe.2025.114481

Publication date
2025

Document Version
Final published version

Published in
Journal of Building Engineering

Citation (APA)
Zhang, H., Song, S., Jiang, N., Feng, Y., Qin, J., Ge, Z., & Šavija, B. (2025). Influence of constituent material on behavior of auxetic cellular composites. *Journal of Building Engineering*, *114*, Article 114481. https://doi.org/10.1016/j.jobe.2025.114481

Important note
To cite this publication, please use the final published version (if applicable).
Please check the document version above.

Copyright
Other than for strictly personal use, it is not permitted to download, forward or distribute the text or part of it, without the consent of the author(s) and/or copyright holder(s), unless the work is under an open content license such as Creative Commons.

Takedown policy
Please contact us and provide details if you believe this document breaches copyrights.
We will remove access to the work immediately and investigate your claim.

This work is downloaded from Delft University of Technology.
For technical reasons the number of authors shown on this cover page is limited to a maximum of 10.

Green Open Access added to TU Delft Institutional Repository
as part of the Taverne amendment.

More information about this copyright law amendment
can be found at https://www.openaccess.nl.

Otherwise as indicated in the copyright section:
the publisher is the copyright holder of this work and the
author uses the Dutch legislation to make this work public.

Journal of Building Engineering 114 (2025) 114481

Contents lists available at ScienceDirect

Journal of Building Engineering

journal homepage: www.elsevier.com/locate/jobe

Influence of constituent material on behavior of auxetic cellular composites

Hongzhi Zhang [a], Shuai Song [a], Nengdong Jiang [a], Yujie Feng [a], Jin Qin [a], Zhi Ge [a,*], Branko Šavija [b]

[a] School of Qilu Transportation, Shandong University, 250002, Jinan, PR China
[b] Faculty of Civil Engineering and Geosciences, Delft University of Technology, 2628 CN, Delft, the Netherlands

ARTICLE INFO

Keywords:
Auxetic cellular structure
Finite element method
Constituent material
Auxetic behavior
Energy absorption

ABSTRACT

This study investigates the influence of the deformability and fracture energy of the constituent material on the compressive response of auxetic cellular composites, using the finite element method (FEM) in ABAQUS/Explicit (version 2019). Four constitutive models were implemented: elastic-brittle, ideal elastic-plastic, strain-hardening, and strain-softening. The unit cell model was validated numerically against a larger 4 × 4 cellular structure and experimentally using strain-hardening cementitious composites with various deformability. Results show that auxetic behavior is unattainable with elastic-brittle constituent materials. For ideal elastic-plastic and strain-hardening materials, increasing the deformability and/or fracture energy leads to a larger critical strain, defined as the strain at which Poisson's ratio recovers from negative to zero under compression. Conversely, strain-softening materials exhibit the opposite trend. For structures comprising three ductile constituents, both load-bearing capacity and energy absorption performance improve with enhanced material properties, most notably for the strain-hardening material. However, a key finding is that increasing the deformability or fracture energy of the constituent material causes a significant reduction in the ratio of energy absorption of the structure to that of its constituent material. This indicates that merely enhancing the deformability and fracture energy of the constituent material does not guarantee improved energy absorption of cellular composites, demonstrating that optimal design of cellular composites requires a synergistic balance between the material and structure, rather than solely maximizing material properties. These insights provide critical guidance for designing high-performance auxetic cellular composites.

1. Introduction

Poisson's ratio is the ratio of transverse contraction strain to longitudinal extension strain in the direction of stretching force. The Poisson's ratio of most well-known materials is positive, generally between 0 and 0.5. These conventional materials expand (shrink) perpendicular to the direction of the applied load (i.e., the cross-section direction) under uniaxial compression (or tension), while materials with negative Poisson's ratio, generally termed as auxetic materials, do the opposite: they shrink (or expand) laterally [1,2]. This unique behavior provides auxetics with various enhanced mechanical properties, such as high energy absorption [3,4], high shear

* Corresponding author.
E-mail address: zhige@sdu.edu.cn (Z. Ge).

https://doi.org/10.1016/j.jobe.2025.114481
Received 16 January 2025; Received in revised form 12 October 2025; Accepted 26 October 2025
Available online 28 October 2025
2352-7102/© 2025 Elsevier Ltd. All rights are reserved, including those for text and data mining, AI training, and similar technologies.

resistance [5,6], and high indentation resistance [7,8]. Auxetics have a broad range of potential applications, including infrastructures for impact resistance [9] and shock absorption [10], as well as biomedical applications [11,12].

Some natural auxetic materials have been identified, including minerals with specific crystal structures (e.g., cubic metals [13], rippled graphene [14], siliceous zeolite MFI-silicalite [15], and crystalline SiO_2 [16]), as well as biomaterials such as cancellous bone from the proximal tibial epiphysis [17], cow teat skin [18], nuclei of naive mouse embryonic stem cells [19], and chromatin gels [20]. On the other hand, artificial auxetic materials have been designed based on periodic 2-D geometries and structures. Holes are commonly introduced to disturb the strain/stress field and allow local rotations. Typical cellular structures with auxetic behavior include concave polygon structures [21,22], rotating polygon structures [23,24], chiral structures [25–27], origami structures [28,29], and double-arrowed structures [30,31]. In general, the density of cellular auxetic materials is significantly lower than that of the constituent materials. The mechanical properties of such materials can be tailored by designing the geometry of the cellular structure [32,33]. Kolken et al. [34] studied the influence of geometric parameters of a titanium re-entrant hexagonal honeycomb on the compression fatigue performance. The auxetic titanium re-entrant hexagonal honeycomb showed exceptional fatigue performance, which increased the possibility of application of auxetic meta-biomaterials in load-bearing field. Master and Evans [35] evaluated the elastic constants of honeycombs by considering the deformation of re-entrant cells (including bending, stretching and hinging), and derived expressions for the tensile modulus, shear modulus, and Poisson's ratio. Xu et al. [36,37] studied the influence of aspect ratio on the compressive behavior of auxetic cementitious cellular composites. The results show that the properties of the cementitious cellular composites are tunable and can be improved by modifying the cellular structure. Berinskii [38] found that the change of the angle between the joints triggers a structure switch from re-entrant to regular honeycomb case, leading to a qualitative change of the mechanical properties. Based on the finite element method (FEM) and interpretable machine learning, Lyngdoh et al. [39] successfully linked the design parameters of auxetic cementitious cellular composites (such as the volume fraction and aspect ratio of voids) to the desired auxetic behavior.

The influence of constitutive model selection on the mechanical behavior of cellular structures has been extensively studied using various modeling approaches. White et al. [40] employed a reduced order model to simulate the macroscopic response of micro-architected cellular structures, demonstrating its efficacy in predicting deformation and stress distributions within non-uniform lattices. Xu et al. [36] implemented a concrete damage plasticity model (CDPM) in ABAQUS/Explicit to analyze the compressive response of auxetic cementitious cellular composites (ACCCs), effectively capturing their uniaxial compression behavior, evolution of Poisson's ratio, and full stress-strain characteristics. In a study on additively manufactured variable-section polylactic acid cellular structures, Li et al. [41] utilized an elastic-ideal plastic constitutive model in ABAQUS/Explicit to simulate quasi-static compression responses. The model accurately reproduced the elastic deformation and global deformation modes. Similarly, Shuang et al. [42] investigated a 3D-printed carbon fiber cellular structure under quasi-static tension using an elastic-ideal plastic model in ABAQUS/Explicit without considering the failure parameters. Their simulations exhibited strong correlation with experimental measurements throughout the elastic-plastic stage, effectively predicting deformation patterns, load-displacement response, and energy absorption. Notably, the majority of these numerical studies were conducted using ABAQUS/Explicit, and despite differences in constitutive models, all approaches successfully captured the expected macroscopic mechanical behavior.

The mechanical response of the negative Poisson's ratio honeycomb structure depends not only on the geometry of the cell elements and their spatial arrangement, but also on the constituent material. For practical applications, different constituent materials have been employed, such as metals [43], silicone rubber [44], cementitious materials [37], as well as graphene and carbon nanotubes [45]. Although it is well established that constituent material significantly influences the universal behavior of the cellular structure, only a few studies have focused on this issue. Recent studies have shown that when the constituent material changes from elastomer to metal, the auxetic behavior caused by buckling due to local plastic deformation disappears [46]. Ren, Hedayati et al. [47] found that octagonal honeycombs made of polylactic acid (PLA) did not exhibit auxetic behavior, but those made of thermoplastic polyurethane elastomer (TPU) showed negative Poisson's ratio characteristics [48]. This indicates that auxetic behavior is controlled by the constituent material: TPU leads to much easier occurrence of square rotation and bending of the cell walls during compression, whereas PLA is relatively stiffer [49]. This was also confirmed by the compression of TPU and PLA arrowhead honeycombs [50]. Additionally, incorporating strain-rate sensitive materials as filler in honeycomb structures results in significant alterations in the evolution of Poisson's ratio and specific energy absorption [51]. Studies on ACCCs with varying fiber contents have revealed that their auxetic behavior, which is attributed to a crack bridging effect, requires the fiber-matrix interfacial slip strength to exceed a critical value [37]. While these findings clearly underscore the significant influence of the constituent material on the auxetic behavior of cellular structures, the fundamental governing factor is its constitutive relationship, which mathematically describes the intrinsic material properties and controls nonlinear deformation and damage progression. Brittle constitutive behavior typically leads to cell separation rather than auxetic deformation [37]. Consequently, research on the effect of material constitutive models on auxetic structures has primarily focused on elastoplastic systems. Xie et al. [52] fabricated elliptical ACCCs using strain-softening, long-tail strain-hardening, and short-tail strain-hardening fiber-reinforced cementitious materials. Their results indicated that, in comparison to strain-softening ACCCs, those with strain-hardening characteristics exhibited higher load-bearing capacity, enhanced energy absorption, and more stable auxetic behavior. Although long-tail strain-hardening ACCCs showed lower strain-hardening than the short-tail counterparts, the latter demonstrated greater recoverable deformation elasticity due to their extended softening capacity. Kucewicz et al. [53] found that the elastic-plastic material model with a nonlinear hardening rule and the elastic-viscoplastic model with damage effects such as softening (reduction in material stiffness) have significantly different quasi-static compression responses. The honeycomb structures composed of elastic-plastic materials are more prone to brittle fracture and rapid crushing. Nevertheless, despite these valuable contributions, a systematic understanding of how the constituent materials with different constitutive relationships govern the auxetic behavior and overall mechanical performance remains largely unexplored. This gap is particularly evident in the lack of controlled

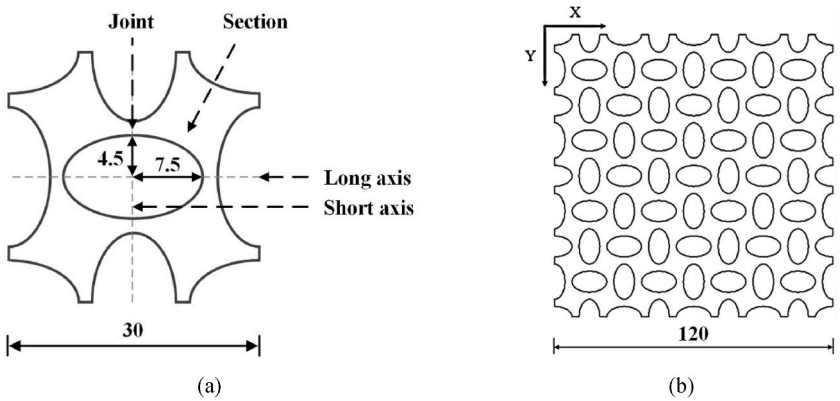

Fig. 1. Geometries of (a) unit cell and (b) 4 × 4 cellular structure (unit: mm).

Table 1
Material input parameters.

Parameters	Value
Density (kg/m^3)	2000
Elastic modulus (MPa)	20000
Poisson's ratio	0.2

comparisons where materials are designed to isolate the effects of their post-yield behavior (e.g., hardening versus softening) while being objectively compared on a common basis, such as equal deformability or equal fracture energy.

To bridge this gap, this study numerically investigated the effect of the constitutive relationship on the mechanical behavior of an auxetic cellular structure. Four classical types of materials, i.e., elastic-brittle, ideal elastic-plastic, strain-hardening, and strain-softening materials, were systematically compared based on two rigorous criteria: identical ultimate deformability and identical fracture energy. This approach allowed a direct and unbiased assessment of how post-yield behavior governs key performance metrics for the first time, including the stress-strain response, macroscopic Poisson's ratio, energy absorption capacity and energy absorption efficiency. Simulations were conducted using ABAQUS/Explicit (2019) on a unit cell model, with validation provided through a larger 4 × 4 cellular structure model and experimental tests on cellular samples fabricated from strain-hardening cementitious materials with different deformation capacities. The consistency between numerical and experimental results confirms the reliability and representativeness of the unit cell model.

2. Materials and methods

2.1. Geometry of cellular structure

The geometric characteristics of the studied unit cell are illustrated in Fig. 1 (a). The auxetic cellular geometry, which features an elliptical hole, was selected for its well-documented ability to exhibit pronounced auxetic behavior through the rotation of its constituent sections [37,54]. The single unit cell consists of four sections, with each side containing two grooves. The shape of each groove is 1/4 of the elliptical hole. When the four sections are assembled into a unit cell, an elliptical hole is formed in the center. The ratio of the long axis to the short axis is fixed as 5:3. This specific aspect ratio was adopted from Xu et al. [36], as it was found to provide an optimal balance between achieving significant auxetic deformation and maintaining structural stability. The unit cell dimensions of 30 mm × 30 mm were selected for numerical analysis based on considerations of computational efficiency and the fact that the normalized mechanical response is determined by the relative geometry rather than the absolute size. Therefore, the results from this model are generalizable to geometrically similar structures at other scales. Furthermore, to validate the accuracy and applicability of the model, a larger periodic structure comprising a 4 × 4 array of unit cells (Figs. 1b and 120 mm × 120 mm) was simulated and benchmarked against the single cell results. The 4 × 4 array was chosen as it is sufficiently large to capture the interactions between unit cells and to reliably validate the representativeness of the single unit cell model.

2.2. Model description

The CDPM in ABAQUS was used to model the constitutive relationship of the four constituent materials, which were assumed to be isotropic. The constitutive equation of CDPM [55] can be expressed as follows:

$$\sigma = (1-d)E_0\left(\varepsilon - \varepsilon^{pl}\right) \tag{1}$$

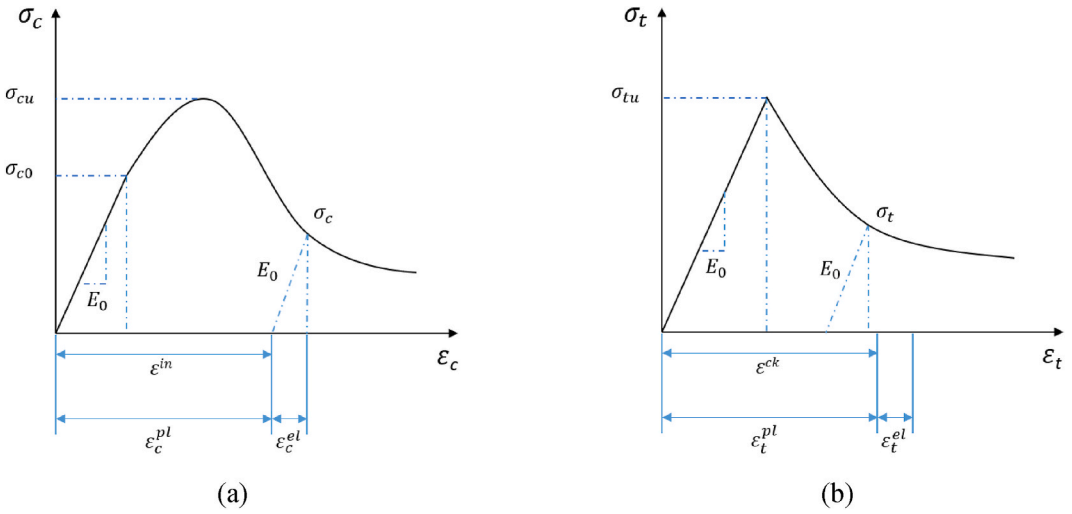

Fig. 2. Definition of CDPM (a) uniaxial compression and (b) uniaxial tension behaviour.

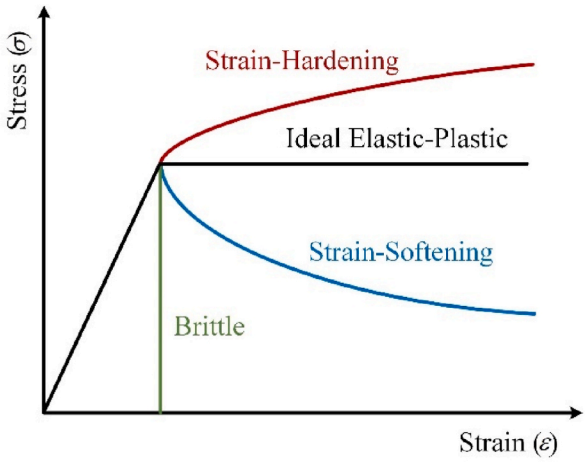

Fig. 3. The adopted 4 typical constitutive relationships.

Where σ denotes the Cauchy stress; ε and $\varepsilon^{\mathrm{pl}}$ represent total and equivalent plastic strain, respectively; E_0 represents the initial elastic modulus. Under modulus reduction, d is the damage variable, which ranges from 0 (undamaged) to 1(fully damaged).

The input parameters for the constituent material include density, elastic modulus, and Poisson's ratio (see Table 1). The uniaxial compressive and tensile responses were characterized by plasticity, with failure evolution controlled by the compressive plastic strain (ε_c^{pl}) and the tensile plastic strain (ε_t^{pl}), respectively. These variables were derived from the uniaxial loading behavior of the material (Fig. 2). In compression, the failure stress (σ_{co}) corresponds to the onset of micro-cracking of the cementitious material after the elastic phase. Under tension, the failure stress (σ_{tu}) corresponds to the ultimate tensile strength. The compressive inelastic strain (ε^{in}) and the tensile cracking strain (ε^{ck}) are defined as the difference between the total strain and the elastic strain of the undamaged material, respectively.

In this study, stiffness degradation was not considered due to the monotonic loading condition without any unloading process. Consequently, the damage parameters typically used to capture elastic modulus degradation during unloading were not defined. In accordance with the CDPM constitutive relationship, it was assumed that the compressive inelastic strain and tensile cracking strain were equated to the plastic strain indicative of damage [36]. To explicitly simulate the cracking of materials, the element deletion technique available in ABAQUS/Explicit was employed. This technique removes an element from the mesh once its equivalent plastic strain exceeds a critical failure strain [56], which is defined by the ultimate deformability of the constituent material (as specified in Section 2.3). This approach allows the model to realistically capture the loss of load-bearing capacity in fractured regions and the evolution of crack patterns throughout the compression process.

Table 2
The plastic parameters of all specimens with different deformability.

Specimen ID	Constitutive relation	Ultimate tensile stress (MPa)	Deformability (%)	Fracture energy (kJ/m^3)
EP1	Ideal Elastic-Plastic	5	1	50
EP2		5	2	100
EP4		5	4	200
EP6		5	6	300
EP8		5	8	400
EP10		5	10	500
SH1	Strain-Hardening	5.3	1	51.5
SH2		5.6	2	106
SH4		6.2	4	224
SH6		6.8	6	354
SH8		7.4	8	496
SH10		8	10	650
SS1	Strain-Softening	4.7	1	48.5
SS2		4.4	2	94
SS4		3.8	4	176
SS6		3.2	6	246
SS8		2.6	8	304
SS10		2	10	350

Table 3
The plastic parameters of all specimens with different fracture energies.

Specimen ID	Constitutive relation	Ultimate tensile stress (MPa)	Deformability (%)	Fracture energy (kJ/m^3)
EP50	Ideal Elastic-Plastic	5	1	50
EP100		5	2	100
EP200		5	4	200
EP300		5	6	300
EP400		5	8	400
EP500		5	10	500
SH50	Strain-Hardening	5.292	0.972	50
SH100		5.568	1.893	100
SH200		6.083	3.609	200
SH300		6.557	5.191	300
SH400		7	6.667	400
SH500		7.416	8.054	500
SS50	Strain-Softening	4.690	1.032	50
SS100		4.359	2.137	100
SS200		3.606	4.648	200
SS300		2.646	7.847	300

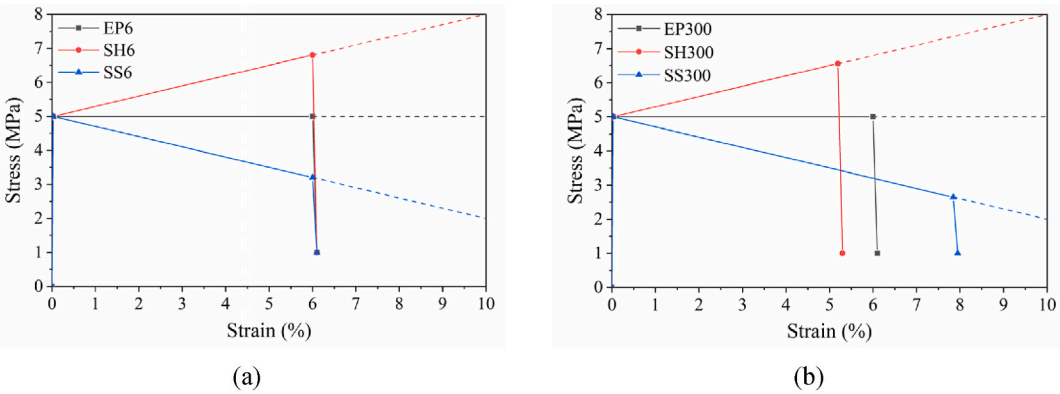

Fig. 4. Comparison of three ductile constitutive relations under (a) the same deformability and (b) the same fracture energy.

2.3. Constitutive relationships of the constituent materials

To systematically investigate the influence of post-yield material behavior on the auxetic response of the cellular structure, respectively, four idealized materials were employed: elastic-brittle, ideal elastic-plastic, strain-hardening, and strain-softening

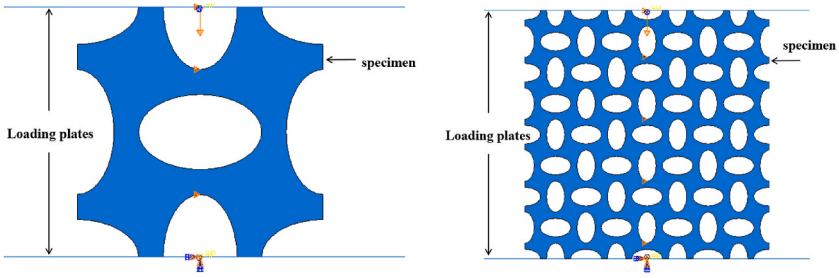

Fig. 5. Two-dimensional uniaxial compression model: (a) unit cell and (b) cellular structure.

materials (Fig. 3). For the elastic-brittle material, when the peak stress is reached, the material fails and the load-bearing capacity drops rapidly to zero. The ideal elastic-plastic, strain-hardening, and strain-softening materials have the same modulus and yield stress in the elastic stage. This approach enables a controlled parametric study by decoupling deformability and fracture energy—two commonly intertwined properties in real materials. Each model corresponds to a representative class of engineering materials: elastic-brittle behavior exemplifies ceramics [57] and glasses [58]; ideal elastic-plastic response is typical of ductile metals [59]; strain-hardening characterizes high-performance composites such as SHCC [60] and certain metals [61]; and strain-softening is representative of quasi-brittle materials like rock [62] and plain concrete [63]. The adoption of these idealized constitutive relationships yields fundamental insights into how key material properties influence the deformation mechanisms and energy absorption of auxetic cellular structures.

Two series of constituent materials were designed for comparison. Firstly, six ultimate tensile strain levels, namely 1 %, 2 %, 4 %, 6 %, 8 % and 10 % were designed for the elastic-plastic constituent materials as references, with fracture energy of 50 kJ/m^3, 100 kJ/m^3, 200 kJ/m^3, 300 kJ/m^3, 400 kJ/m^3 and 500 kJ/m^3 respectively. The design parameters of ultimate tensile stress, ultimate tensile strain, and fracture energy of three constituent materials are shown in Tables 2 and 3. In the first series, the three constituent materials were defined based on the 6 levels of deformability. For example, Fig. 4 (a) compares the constitutive relationship of ideal elastic-plastic (EP6), strain hardening (SH6), and strain softening (SS6) materials, with an ultimate tensile strain of 6 %. With the same deformability, the three constituent materials have different fracture energies. In the second series, six levels of fracture energy were used to define the constitutive relationships. Fig. 4 (b) shows the constitutive relationships of the three constituent materials (EP300, SH300, SS300) with a fracture energy of 300 kJ/m^3. Note that the EP300 is the same as EP6, the yield stress is controlled to 5 MPa to compare the effect of deformability and fracture energy on cellular structure. The plastic parameters, concluding yield stress and plastic strain, were derived from the constitutive relationships.

2.4. Model settings

The compressive behavior of the unit cell and cellular structure was simulated using the commercial finite element package (ABAQUS/Explicit). Geometric nonlinearity was considered in the analyses. In order to minimize the computational effort, two-dimensional (2D) models were used. Previous studies have shown that cellular structures do not exhibit buckling behavior [36,39]. Therefore, this 2D plane stress model adopts a unit out-of-plane thickness to simplify the analysis of in-plane behavior. The built-up models are shown in Fig. 5.

The first step involved generating the two-dimensional unit cell (30mm × 30 mm) and the cellular structure (120mm × 120 mm), respectively. Two loading platens (two-dimensional planar discrete rigid) were arranged at the top and bottom of the specimen. Reference points were created at the center of each platen. To account for the interaction between solid surfaces, the surface-to-surface contact between the specimen and loading platens as well as the self-contact of the specimen were defined. The tangential friction between the specimen and the loading platens was set to zero. As the elements of the specimen come into contact with one another after compressive failure and deformation, a friction coefficient of 0.9 was assumed as the self-contact parameter. This high value was adopted to simulate the significant mechanical interlocking and resistance between fractured, rough material surfaces during large deformation and compaction, rather than the kinetic friction between smooth surfaces [64,65]. Moreover, studies have shown that the stress-strain response is not highly sensitive to the specific value of the self-contact friction coefficient within a high range ($\mu \geq 0.5$) [65].

A displacement-controlled loading protocol was applied by prescribing a vertical displacement of 30 % of the specimen height (40 % for the cellular structure test) to the upper loading platen, while constraining all its other degrees of freedom. The bottom platen was fully fixed in all directions. To meet the requirements of large deformation and contact analysis, 6-node modified quadratic plane stress triangle elements (CPS6M) were used.

2.5. Model reliability

2.5.1. Element size

The selection of an appropriate mesh size has a vital influence on the simulation of structural deformation under compression,

Table 4
Discretization and computational cost parameters for the mesh sensitivity study.

Mesh size (mm)	Number of elements	Number of nodes	Computational time (h)
0.1	872663	1750521	41
0.2	220130	442920	5.2
0.5	35682	72424	0.8

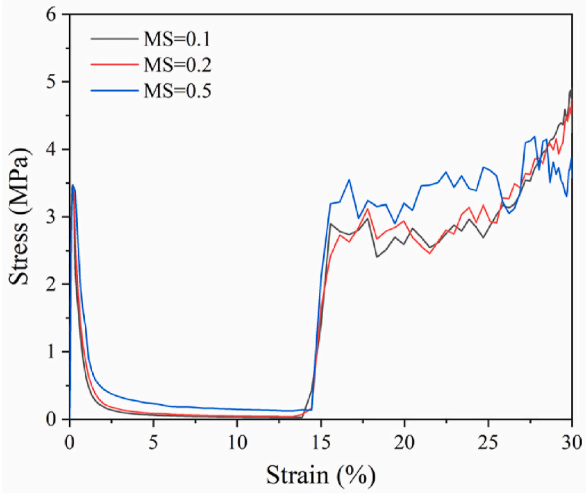

Fig. 6. Simulated stress-strain curves of the unit cell using three element sizes.

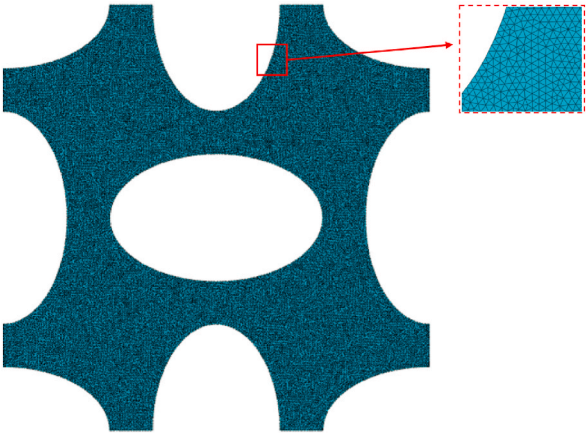

Fig. 7. Meshing diagram of the unit cell specimen.

particularly for capturing the failure process accurately. An excessively fine mesh incurs significantly higher computational costs, while an overly coarse mesh may compromise computational accuracy. Therefore, it is necessary to determine an appropriate mesh size to balance the computational accuracy and cost, and to guarantee the convergence of the solution. Three mesh sizes were selected to simulate the behavior of a single unit cell. They are 0.1, 0.2 and 0.5 mm and are termed as MS = 0.1, MS = 0.2 and MS = 0.5, respectively. For the purpose of comparison, the constituent material (EP6) was used for all three simulations.

Table 4 summarizes the discretization parameters and computational cost for the three meshes. The simulated stress-strain curves are plotted in Fig. 6. The results show a negligible difference between the responses of the MS = 0.2 and MS = 0.1 meshes, indicating that the global mechanical response has converged for a mesh size of 0.2 mm. However, as shown in Table 4, the computational time for the MS = 0.1 mesh was approximately 8 times longer than that for the MS = 0.2 mesh. The MS = 0.5 mesh, while computationally efficient, showed a noticeable deviation in the response. Consequently, the mesh size of 0.2 mm was selected for all subsequent simulations, as it achieves an optimal balance between computational accuracy and efficiency. The meshing diagram of the specimen with the selected mesh size (MS = 0.2) is shown in Fig. 7.

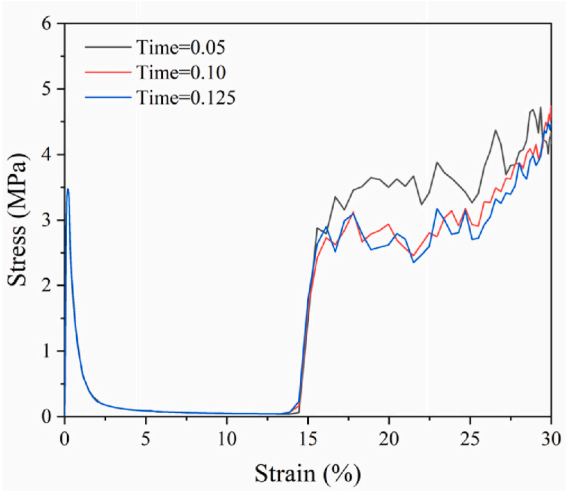

Fig. 8. Simulated stress-strain curves of the unit cell using three time periods.

Table 5
Mix design of SHCC (kg/m^3).

Mixture ID	Cement	Fly ash	Quartz sand	Water	VMA	PCE	Fiber
P1.2	552.0	662.0	440.3	340.0	0.55	7.29	15.6
P1.6	552.0	662.0	440.3	340.0	0.55	7.29	20.8
P1.8	552.0	662.0	440.3	340.0	0.55	7.29	23.4
P2.0	552.0	662.0	440.3	340.0	0.55	7.29	26.0

Note: P1.2 represents a fiber volume fraction of 1.2 %.

Fig. 9. (a) Silicone mold, (b) unit cell specimen, and (c) unit cell specimen with surface-sprayed scattering.

2.5.2. Loading time

In the explicit dynamic analysis, the loading rate (or strain rate) must be carefully selected to approximate quasi-static conditions by minimizing inertial effects. To determine a suitable loading rate, a sensitivity analysis was conducted by varying the total loading time. The average nominal strain rate was calculated as the total nominal strain (30 %) divided by the total loading time.

Three loading times were investigated: 0.05 s, 0.1 s and 0.2 s, which correspond to average nominal strain rates of 6.0 s^{-1}, 3.0 s^{-1} and 1.5 s^{-1}, respectively. The same constituent material (EP6) and mesh size of 0.2 were used for all cases. The simulation results are shown in Fig. 8. The stress-strain curves for loading times 0.1 s and 0.2 s (strain rates of 3.0 s^{-1} and 1.5 s^{-1}) are virtually identical, indicating convergence of the mechanical response and negligible inertial effects at these rates. Therefore, a loading time of 0.1 s (strain rate of 3.0 s^{-1}) was selected for all subsequent simulations. This rate ensures that the conditions are effectively quasi-static while maintaining computational efficiency.

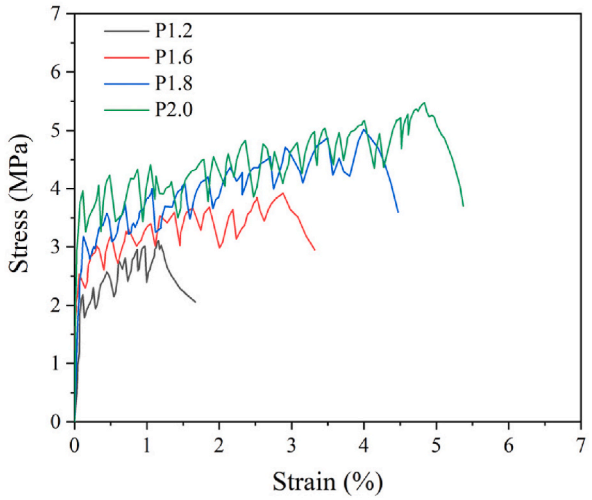

Fig. 10. The tensile stress-strain curves of SHCC with different deformability.

Table 6
The results of uniaxial tension test.

Mixture ID	Initial crack stress σ_t/MPa	Ultimate tensile stress f_{tu}/MPa	Ultimate tensile strain ε_{tu}
P1.2	2.14	3.13	0.012
P1.6	2.52	3.96	0.029
P1.8	3.25	5.05	0.040
P2.0	3.94	5.54	0.049

Table 7
The plastic parameters of SHCC.

Mixture ID	Yield stress (MPa)	Plastic strain (%)
P1.2	2.19	0.00
	2.30	0.14
	2.57	0.29
	2.68	0.43
	2.90	0.64
	3.11	1.00
P1.6	2.53	0.00
	2.92	0.16
	3.12	0.34
	3.42	1.03
	3.66	2.02
	3.92	2.78
P1.8	3.18	0.00
	3.34	0.21
	3.76	0.53
	4.18	1.66
	4.60	2.58
	5.02	3.79
P2.0	3.97	0.00
	4.25	0.39
	4.57	1.96
	4.87	2.37
	5.17	3.90
	5.47	4.68

2.6. Model validation

The strain-hardening materials were chosen to validate the model. Specifically, SHCC was used as the constituent material. The material composition includes P.O 42.5 ordinary Portland cement, Class F fly ash, quartz sand, superplasticizer, viscosity modifying agent (VMA), deionized water, and REC-15 type polyvinyl alcohol (PVA) fiber. The mass ratio of cement to fly ash was 1:1.2 and the

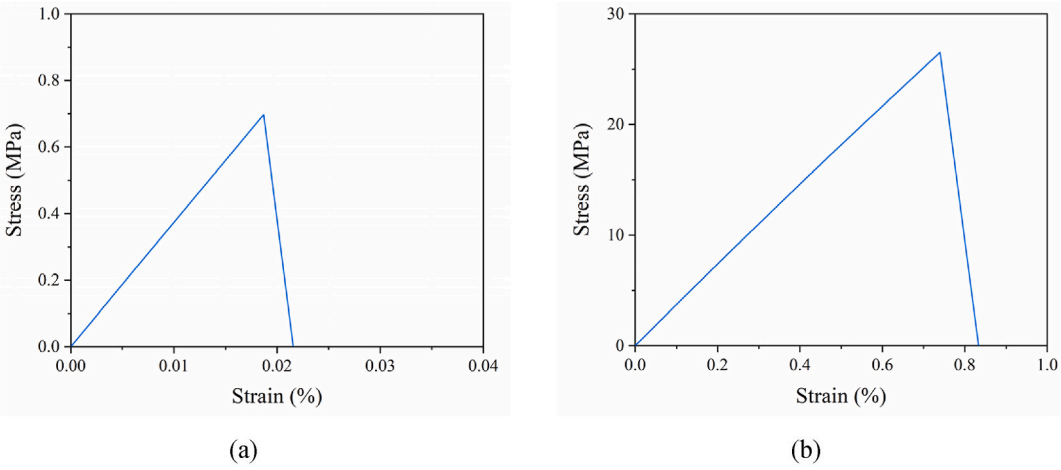

Fig. 11. Stress-strain curve of the unit cell made of elastic-brittle material with the elastic strain of (a) 0.025 % and (b) 1.25 %.

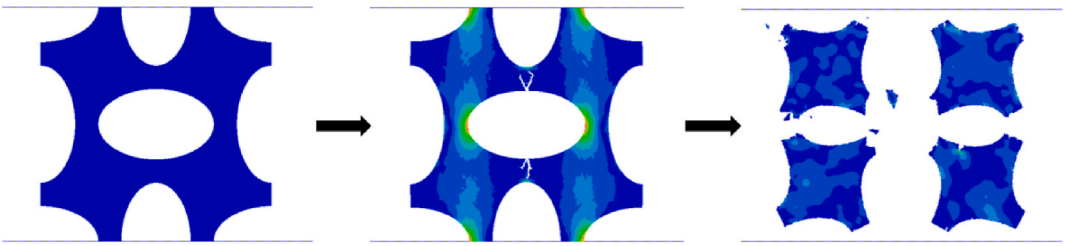

Fig. 12. Failure process of the unit cell made of elastic-brittle constituent material.

water-cement ratio was 0.28. The different deformability of SHCC was achieved by varying the added fiber volume fraction, namely 1.2 %, 1.6 %, 1.8 % and 2.0 %. Table 5 lists the four series of SHCC mix proportions. The unit cell specimens (90 mm × 90 mm) were prepared by pouring SHCC into a silicone mold, as shown in Fig. 9(a) and (b). After 28 days of standard curing, the quasi-static compression test was conducted using a universal loading machine, with a loading rate of 0.01 mm/s. The digital image correlation (DIC) technique was employed to visualize the strain field during the loading process. Before the test, the speckle pattern was applied to the specimen surface for identification and tracking, as shown in Fig. 9 (c). In addition, the upper and lower surfaces of the specimen were polished to ensure that the specimen was uniformly loaded in the axial direction. A thin plastic film was placed on the upper and lower loading plate surfaces to generate a low friction between specimen and loading plates.

To determine the input constitutive relationship of the elastic-plastic model in the FEM, uniaxial tensile tests were conducted on SHCC. Dumbbell specimens with a cross-section of 30 mm × 13 mm were adopted in accordance with the Japan Society of Civil Engineers (JSCE) recommendation [66]. Two linear variable displacement transducers (LVDTs) were employed to measure the tensile deformations within a gauge length of 80 mm, and the loading rate was fixed at 0.1 mm/min. The experimentally measured stress-strain responses (Fig. 10 and Table 6) were used as the benchmark to derive the plastic parameters, as indicated in Table 7.

3. Results and discussion

3.1. Unit cell structure

3.1.1. Responses of unit cell made of elastic-brittle constituent material

Figs. 11 and 12 show the stress-strain curve and failure process of the unit cell made of elastic-brittle constituent material. The stress increases linearly with the strain until reaching the peak stress, followed by a sharp drop. This is associated with the failure of the unit cell. The failure is caused by the rupture of the joints, leading to the separation of the four sections. In addition, another computational compression test was performed by increasing the elastic strain of the material by 50 times (strain at peak = 1.25 %) and keeping the elastic modulus unchanged. Although the unit cell can deform much more than in the previous case, the failure remains brittle. The auxetic behavior is not observed. The results indicate that for the design of auxetic behavior using such structure, elastic-brittle constituent materials should not be considered.

This absence of auxetic behavior is attributed to the fundamental deformation mechanism of elastic-brittle materials. The auxetic behavior of this cellular structure relies on the ductile rotation of the unit cell sections around the joints, a process that generates macroscopic lateral shrinkage. However, the elastic-brittle material, lacking any plastic deformation capacity, cannot accommodate

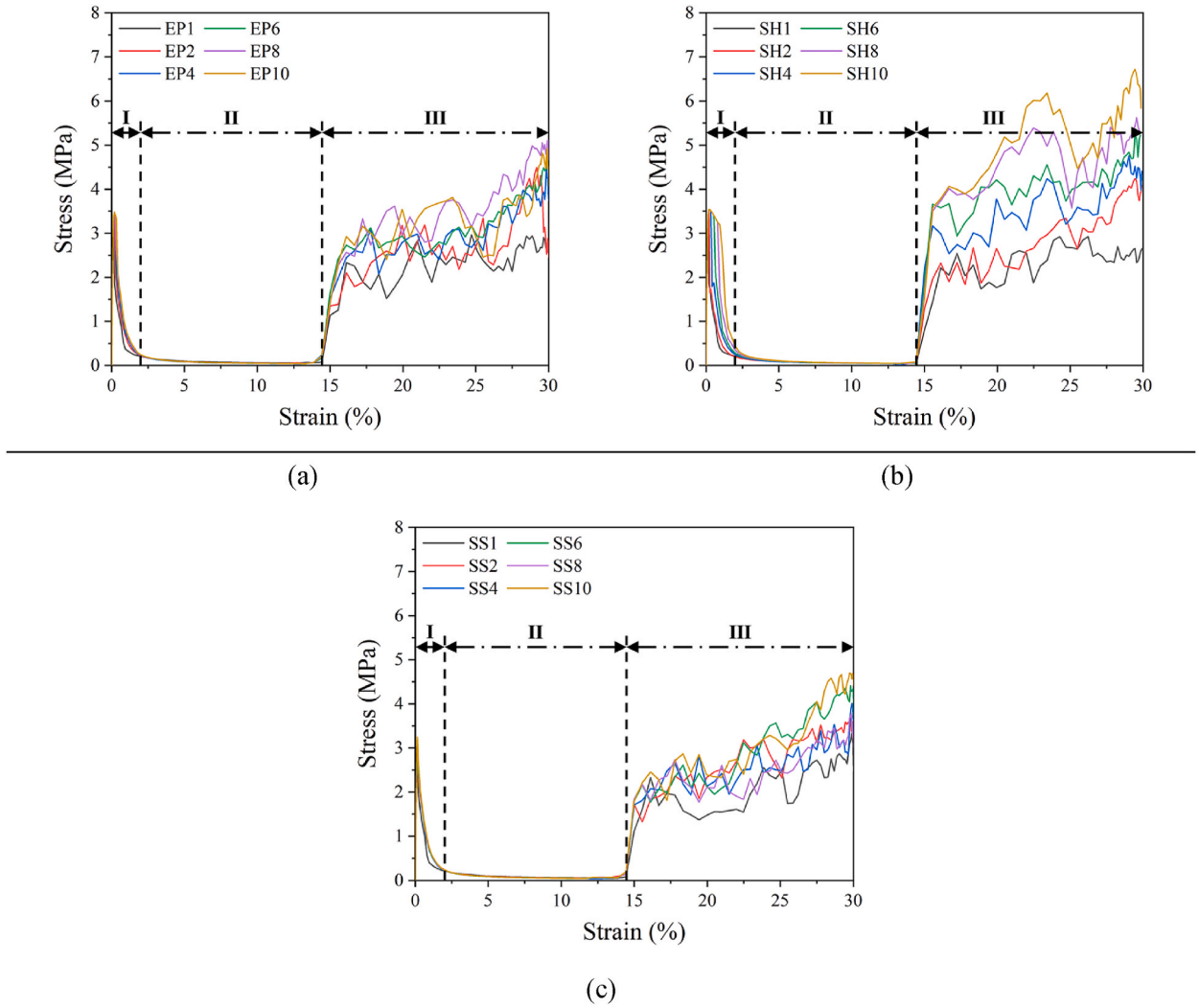

Fig. 13. Stress-strain curves of unit cell specimens made of (a) ideal elastic-plastic, (b) strain-hardening, and (c) strain-softening constituent materials with various deformability.

this required deformation. Upon reaching the ultimate tensile strength, the material at the critically stressed joints undergoes instantaneous catastrophic fracture. This sudden rupture of the joints abruptly releases the stored elastic energy and prevents the sustained, coordinated rotation of the sections that is necessary for achieving a negative Poisson's ratio. Consequently, the structure fails through a brittle, separation mode rather than a progressive, auxetic collapse mode.

3.1.2. Responses of unit cell made of ductile constituent materials

The simulated stress-strain curves were plotted in Figs. 13 and 14. Fig. 15 shows the stress field of the unit cell under various loading stages. The compression process can be divided into three stages. In the first stage (from 0 to about 2 % strain), the compressive stress increases rapidly to the first peak (about 3.5 MPa). This initial peak is primarily governed by the structural elasticity and yielding of the material, which is why similar peak stresses are observed across different ductile materials. Once the first peak is reached, buckling occurs at the joints. The ensuing deformation is facilitated by the ductility of the material, which permits rotation of the sections around the joints, drawing them closer together. Meanwhile, the unit cell begins to shrink laterally and the stiffness decreases significantly. Although the first peak stress remains similar across specimens made of different constituent materials, the post-peak ductility increases with increasing deformability or fracture energy. This enhancement is governed by the material's fracture energy, which impedes micro-crack propagation, thereby prolonging the load-bearing period and permitting greater plastic deformation beyond the peak stress.

The second stage (from 2 % to 14 % strain) exhibits a sustained stress plateau, which characterizes the compaction process of the unit cell. This plateau corresponds to the progressive rotation of the cell sections, which is the fundamental mechanism enabling auxetic behavior. The near-constant stress level is maintained because the energy required to drive the continued rotation and

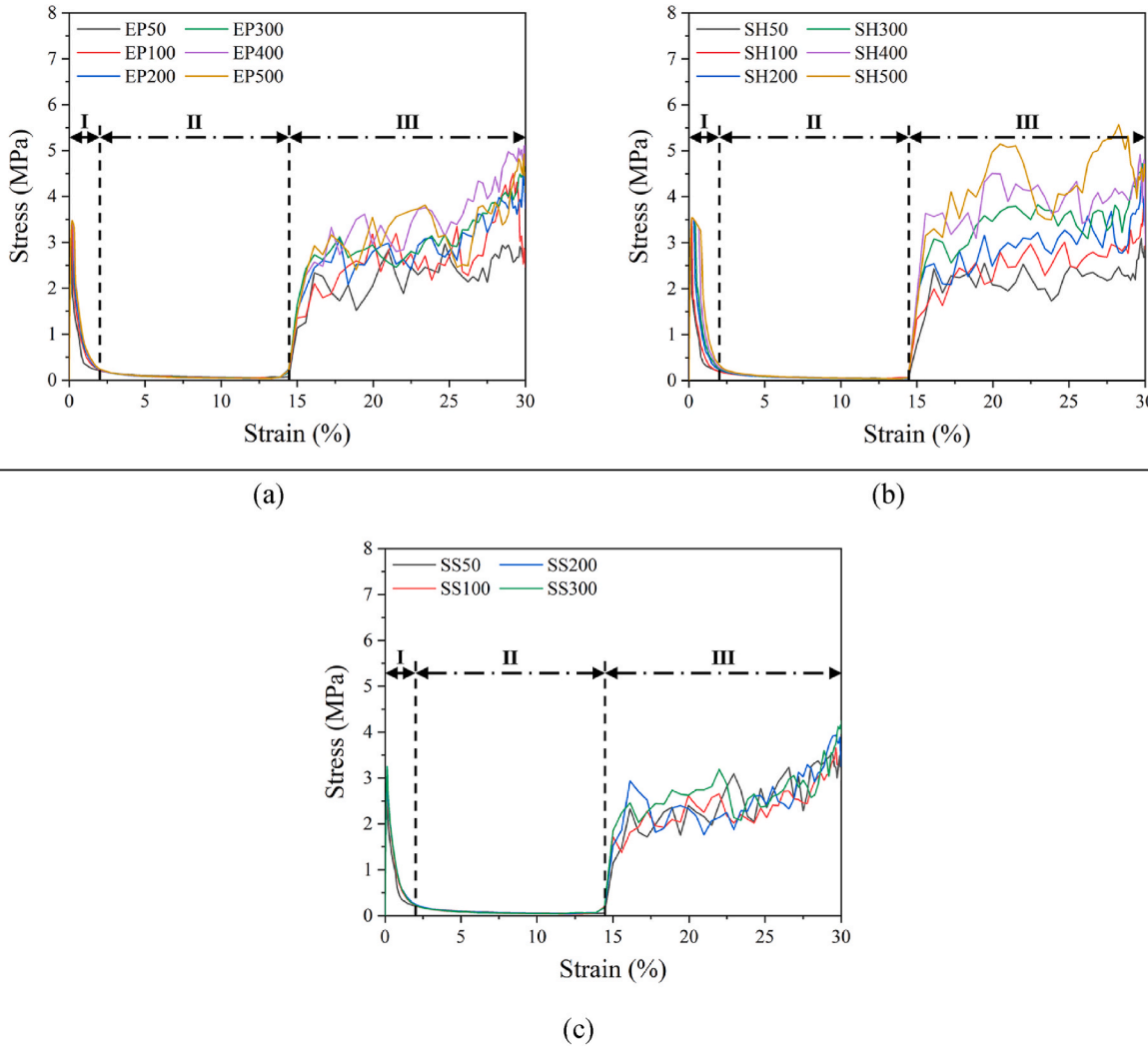

Fig. 14. Stress-strain curves of unit cell specimens made of (a) ideal elastic-plastic, (b) strain-hardening, and (c) strain-softening constituent materials under different fracture energies.

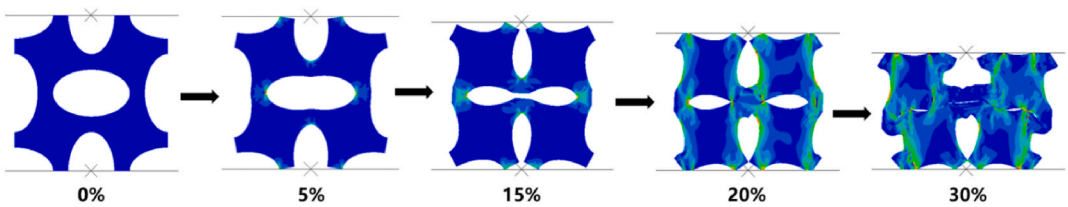

Fig. 15. Compression process of the unit cell (until 30 % strain).

reconfiguration of the sections is balanced by the plastic dissipation of the ductile material at the joints. This stable collapse mode allows the structure to undergo large deformations without a significant increase in load. As compression increases, the sections continue to rotate, and the unit cell continues shrinking laterally. Finally, the four sections come into contact and are squeezed together.

The third stage (from 14 % to 30 % strain) is characterized by the compression failure of the compacted unit cell. The load continues to increase, and the unit cell gradually expands to both sides in the lateral direction, marking the loss of auxetic behavior and the transition to conventional solid-like compression. This three-stage compressive behavior has also been observed in many other cellular structures [43,67].

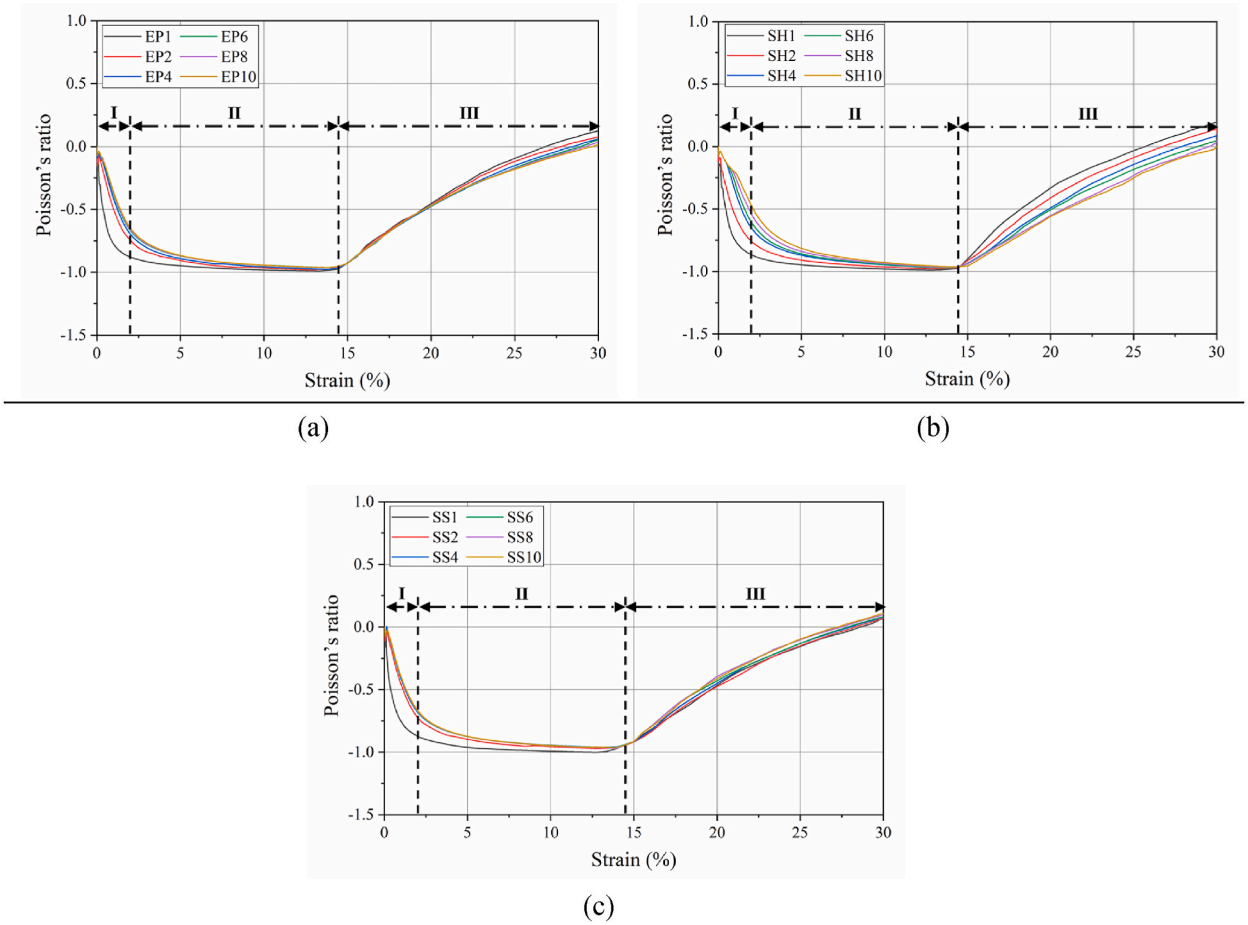

Fig. 16. Poisson's ratio curves of unit cell specimens made of (a) ideal elastic-plastic, (b) strain-hardening, and (c) strain-softening constituent materials with various deformability.

3.1.3. Auxetic behavior of unit cell

The Poisson's ratio of the unit cell was calculated as the ratio of the lateral strain on the outermost edge to the corresponding axial strain. Figs. 16 and 17 show the changes in Poisson's ratio of different specimens at various loading stages. Clearly, two stages can be defined. In the first stage, the unit cell continuously shrinks laterally, and Poisson's ratio decreases until it reaches a minimum at a certain strain, at which the four sections are in contact with each other and the unit cell is completely compacted. The geometrically dominated rotation of the sections determines this minimum value, explaining why it remains approximately −1 regardless of the constituent material. The lower the deformation or fracture energy of the material, the weaker the resistance to transverse contraction. This is because less energy is required to induce plastic hinge formation and section rotation, resulting in faster transverse contraction and initial decreasing rate of the cell. After reaching the minimum Poisson's ratio point, the unit cell begins to expand laterally, and the Poisson's ratio gradually increases. The Poisson's ratio eventually exceeds zero, indicating that the failure of the auxetic structure. The rate of increase in Poisson's ratio varies with the deformability and fracture energy of the constituent materials. Similar behavior has been reported in other structures such as double arrowhead honeycombs [68]. Additionally, it is interesting to mention that a more significant difference is observed in the Poisson's ratio-strain curve with changes of deformability or fracture energy for strain-hardening constituent materials. This is because the sustained hardening response provides continued resistance against the lateral expansion during compaction, thereby delaying the recovery of Poisson's ratio [36].

The critical strain at which the Poisson's ratio of the unit cell transitions from negative to zero is derived and compared in Fig. 18. The larger the critical strain is, the longer the specimens are in the auxetic behavior stage. As can be seen from the figure, the critical strain gradually increases with increasing deformability or fracture energy of elastic-plastic and strain-hardening constituent materials. The increment is more significant for the strain-hardening materials because their increasing load-bearing capacity after yield effectively postpones the full compaction and the consequent lateral expansion. The critical strain of the strain-hardening material becomes the highest among the three types when the deformability exceeds 4 % or the fracture energy exceeds 300 kJ/m^3. The opposite trend is found for the strain-softening material. This is because, for the strain-softening material, the load-bearing capacity decreases with the deformation after the elastic stage. Once the stress exceeds the ultimate strength of the local material (element), deformation continues until the maximum strain is reached, leading to localized failure rather than coordinated structural

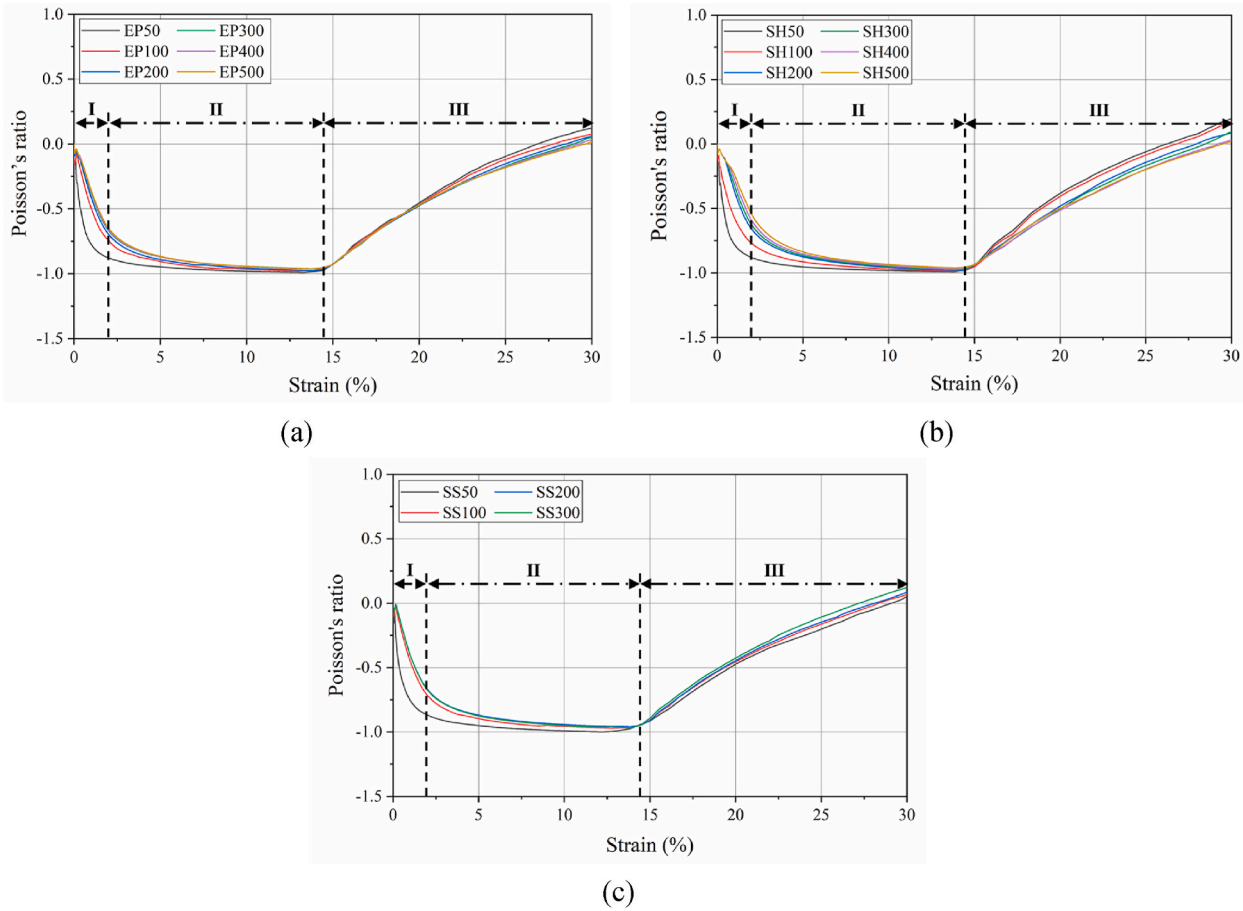

Fig. 17. Change of Poisson's ratio of unit cell made of (a) ideal elastic-plastic, (b) strain-hardening, and (c) strain-softening constituent materials with different fracture energies.

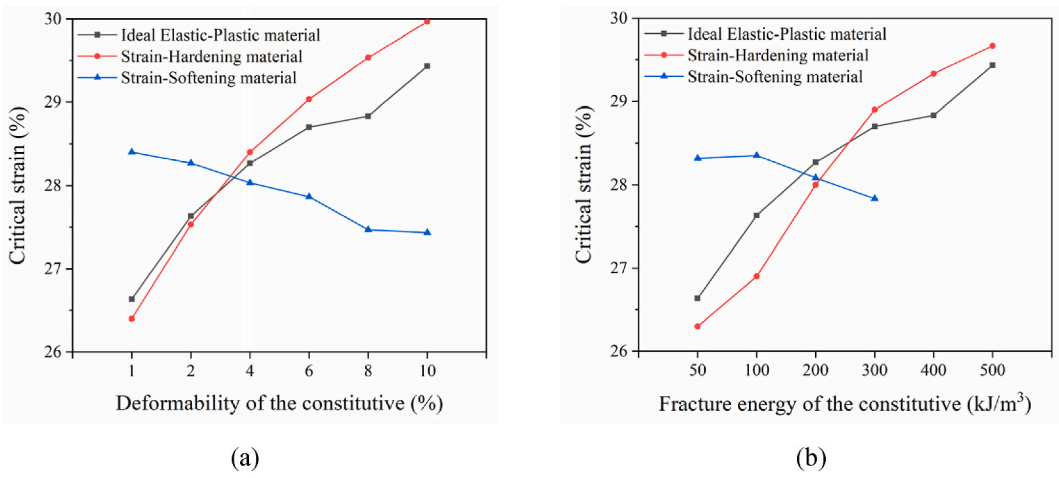

Fig. 18. Influence of (a) deformability and (b) fracture energy of constituent material on the critical strain.

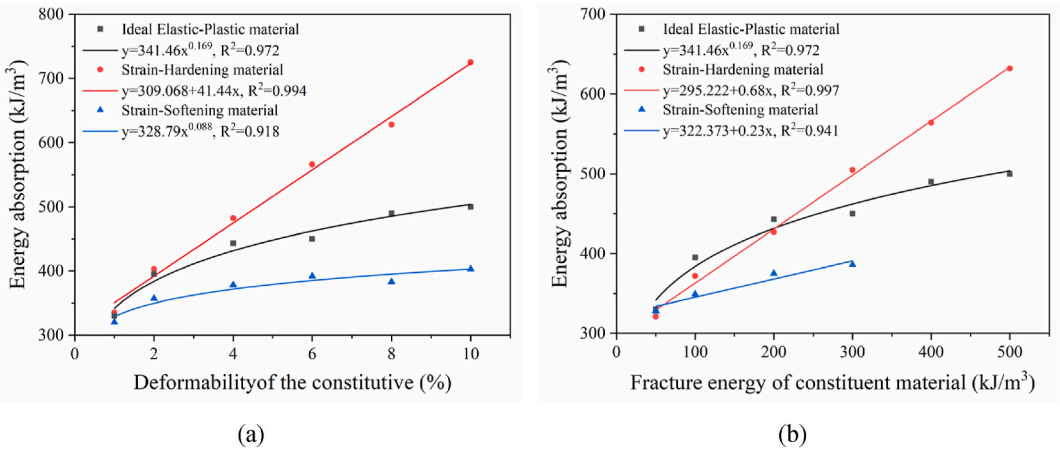

Fig. 19. Influence of (a) deformability and (b) fracture energy of constituent material on energy absorption capacity of unit cell.

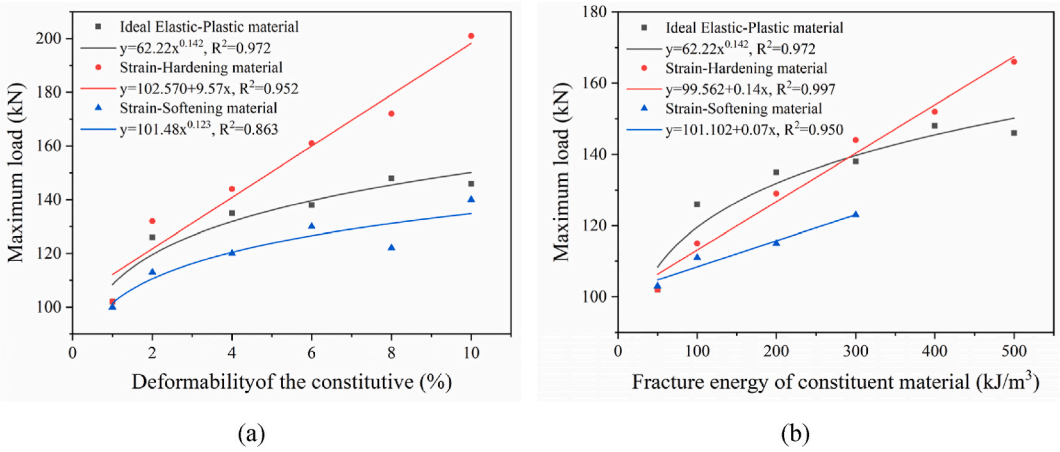

Fig. 20. Influence of (a) deformability and (b) fracture energy of constituent material on the maximum load of unit cell.

deformation. The higher deformability or fracture energy would thus speed up the failure of the auxetic structure by promoting strain localization and disrupting the synergistic rotation of the cellular sections.

3.1.4. Energy absorption and maximum load-bearing capacities

The energy absorption capacity, defined as the energy absorbed per unit volume of cellular solids, was defined by integrating the area under the stress-strain curve [69,70]. Fig. 19 shows the calculated energy absorption capacity. The energy absorption of the unit cell specimens increases with both the deformability and fracture energy of the constituent material. However, the rate of increase varies among different constituent materials. Among them, specimens composed of strain-hardening constituent materials exhibit the highest increase in energy absorption, whereas those made of strain-softening constituent materials show the lowest. This is because the continuous hardening response of strain-hardening materials maintains a higher overall stress level throughout the deformation process, enabling the structure to sustain a higher load over a larger strain range and thus dissipate more energy through extensive plastic deformation [71,72]. In contrast, the strain-softening materials exhibit a reduced load-bearing capacity post-yield due to damage accumulation, leading to lower energy dissipation.

As shown in Fig. 19 (a), the difference in energy absorption among the three constituent materials continues to increase with deformability, and strain-hardening constituent materials always possess the largest energy absorption capacity at a given deformability. The reason may be that, under the same deformability, the strain-hardening materials achieve a higher strength level, which directly translates to a higher fracture energy and a greater area under the stress-strain curve. Regression analysis revealed a linear relationship between the energy absorption and deformability for the strain-hardening material, while power functions were found to describe the behavior of elastic-plastic and strain-softening materials. Fig. 19 (b) compares the energy absorption capacity of unit cells composed of materials with the same fracture energy. When the fracture energy is 50 kJ/m^3, the strain-hardening material leads to the lowest energy absorption capacity because its high strength comes at the expense of limited ductility at this low energy level, restricting the deformation range. However, the energy absorption capacity of the strain-hardening material increases most

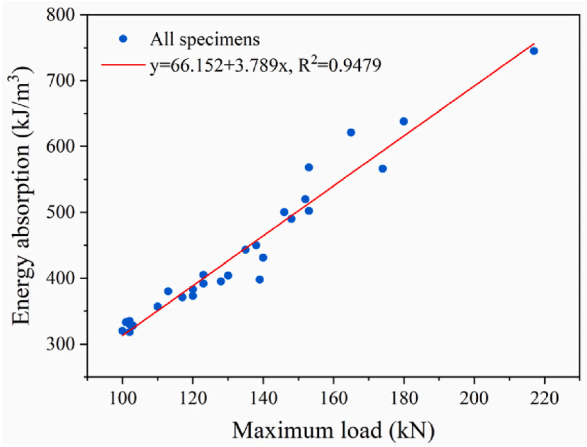

Fig. 21. Relationship between the maximum load and energy absorption capacity of the unit cell.

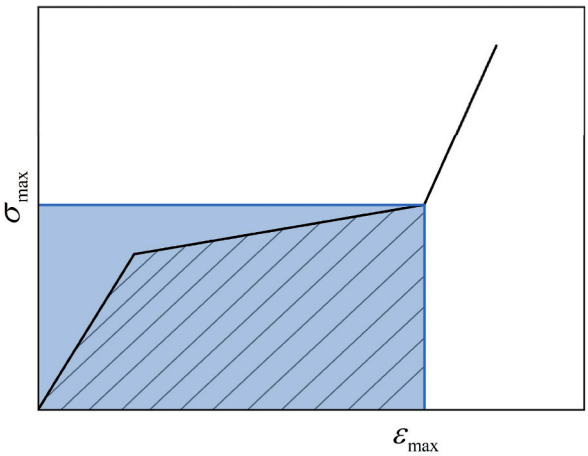

Fig. 22. Schematic view of energy absorption efficiency.

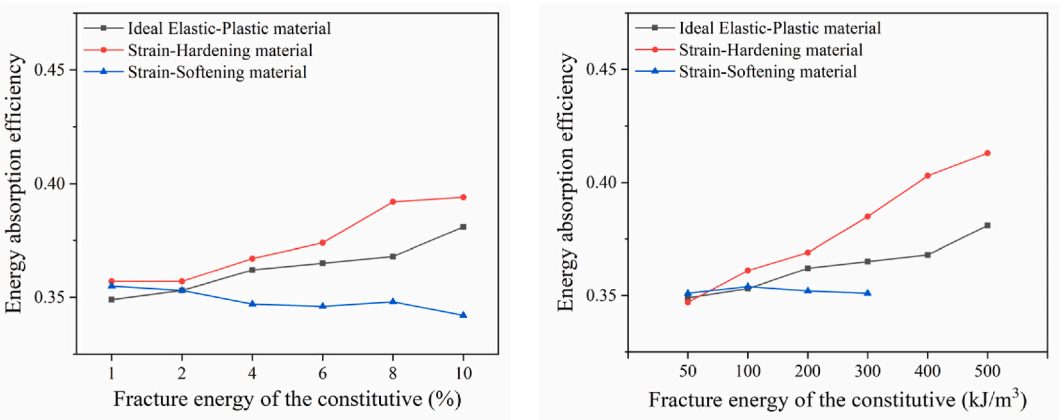

Fig. 23. Influence of (a) deformability and (b) fracture energy of constituent material on the energy absorption efficiency of unit cell.

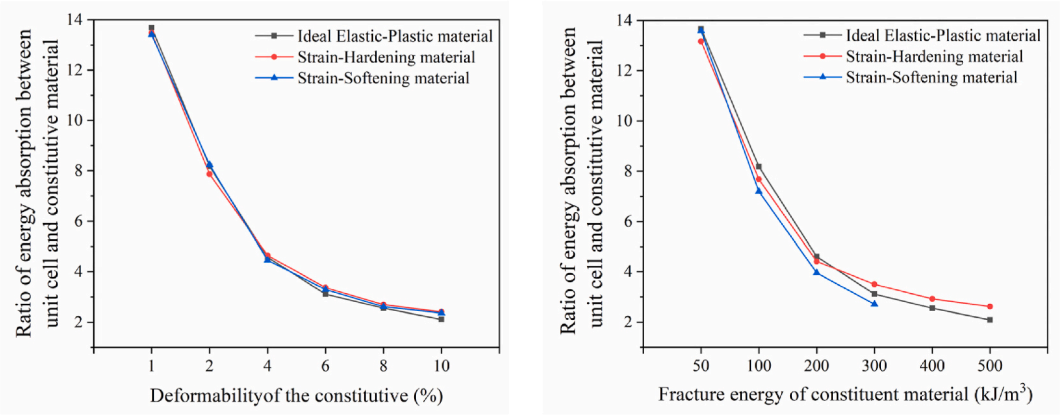

Fig. 24. Influence of (a) deformability and (b) fracture energy of constituent material on the ratio of energy absorption between unit cell and constitutive material.

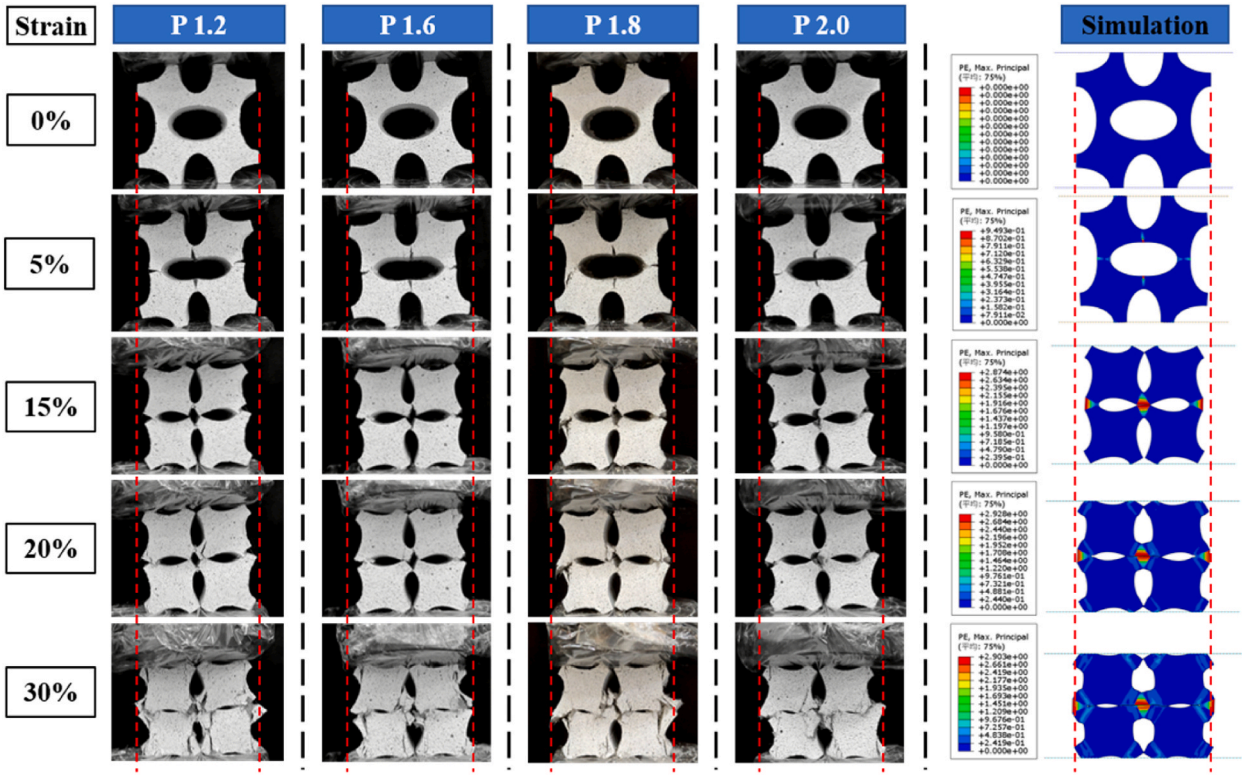

Fig. 25. Comparison of the compression process of unit cell specimens with various deformability under quasi-static compression: experiments and simulation results.

significantly with fracture energy among the three, owing to its unique combination of high strength and enhanced ductility, which creates a synergistic effect leading to superior energy dissipation. It surpasses the elastic-plastic material when the fracture energy reaches 300 kJ/m^3. A linear relationship can be used to express the relationship between the energy absorption and fracture energy for strain-hardening and strain-softening materials, and a power function holds for the elastic-plastic material.

The maximum load that the unit cell can bear during loading (in the range of 30 % strain) is derived from Fig. 13 and plotted in Fig. 20. Clearly, it is consistent with the energy absorption capacity presented in Fig. 19. This indicates that the higher the load the specimen can sustain under the compression process, the more energy it absorbs. The main reason is that increased deformability and fracture energy of the constituent material raise the load required to achieve a given compressive deformation, thereby enhancing the

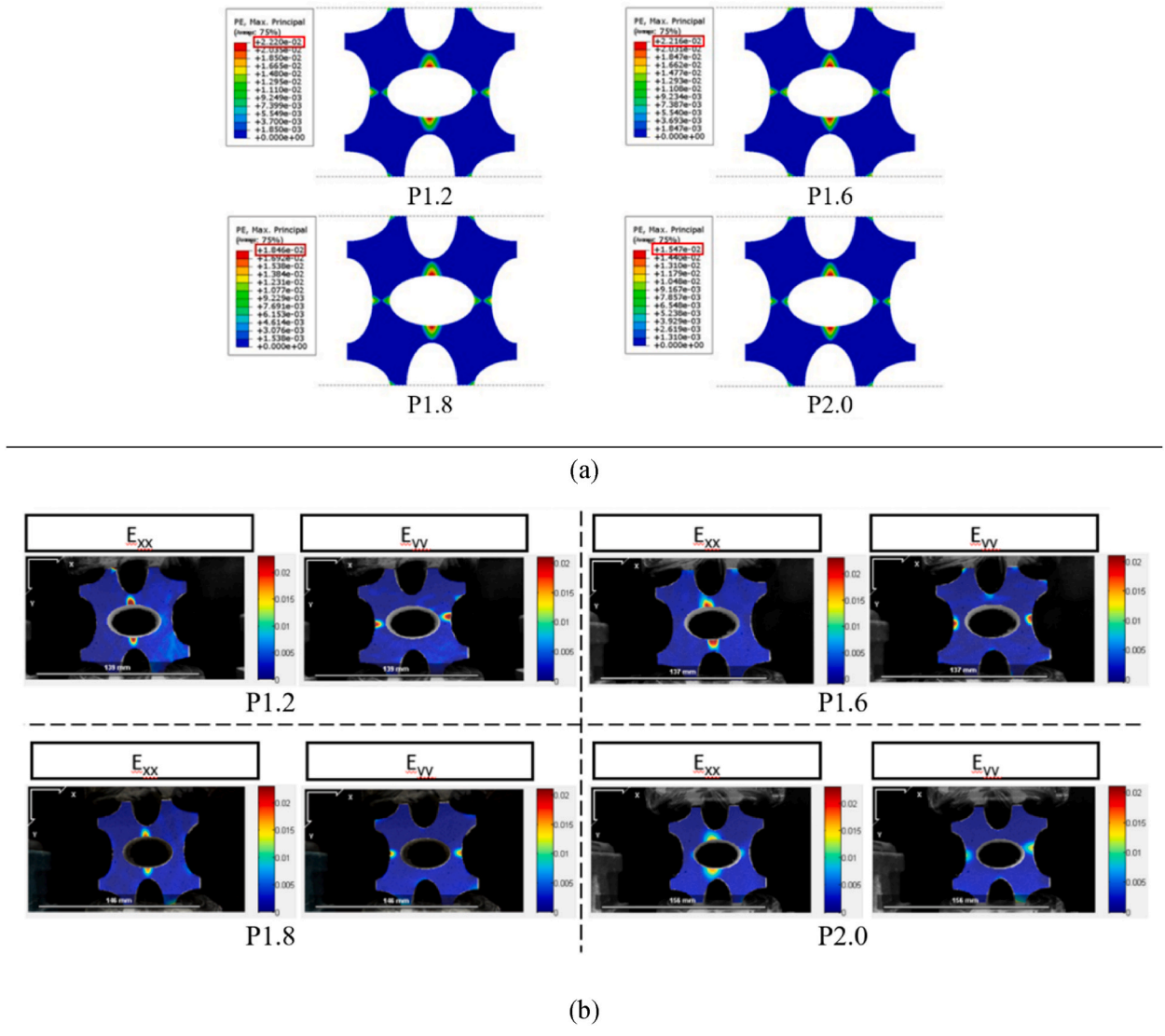

Fig. 26. High local strain region of the unit cell at 5 % compressive strain (a) simulation results, (b) DIC results.

energy absorbed throughout the whole compression process.

Fig. 21 shows the relationship between the maximum load and energy absorption capacity of the unit cell. Evidently, a linear relationship exists between these two parameters. The coefficient of determination R^2 is 0.9479. This indicates that, regardless of the constitutive relationship of the material, a higher load-bearing capacity in stage III always corresponds to a higher energy absorption ability.

3.1.5. Energy absorption efficiency

As shown in Fig. 22, energy absorption efficiency is defined as the ratio of the black shaded area to the blue rectangular area in the stress-strain curve. It is used to determine how close the unit cell is to an ideal energy absorption material whose stress-strain curve corresponds to the blue rectangle [73,74]. The higher the energy absorption efficiency, the closer the material approaches the ideal energy absorption material. Note that σ_{max} is the maximum stress, and ε_{max} is the maximum strain under compression, which is set to 30 % strain in this study.

Fig. 23 compares the energy absorption efficiency of the unit cell made of different constituent materials. It can be seen that the energy absorption efficiency of specimens composed of different materials is comparable when the deformability of the constituent is 1 % or its fracture energy is 50 kJ/m^3. The energy absorption efficiency of specimens made of elastic-plastic and strain-hardening constituent materials increases with the deformability or fracture energy of the constituent material, with a more pronounced increase observed in strain-hardening materials. This trend is consistent with that of energy absorption capacity, as shown in Fig. 19. The high energy absorption capacity generally corresponds to high energy absorption efficiency. Conversely, the energy absorption

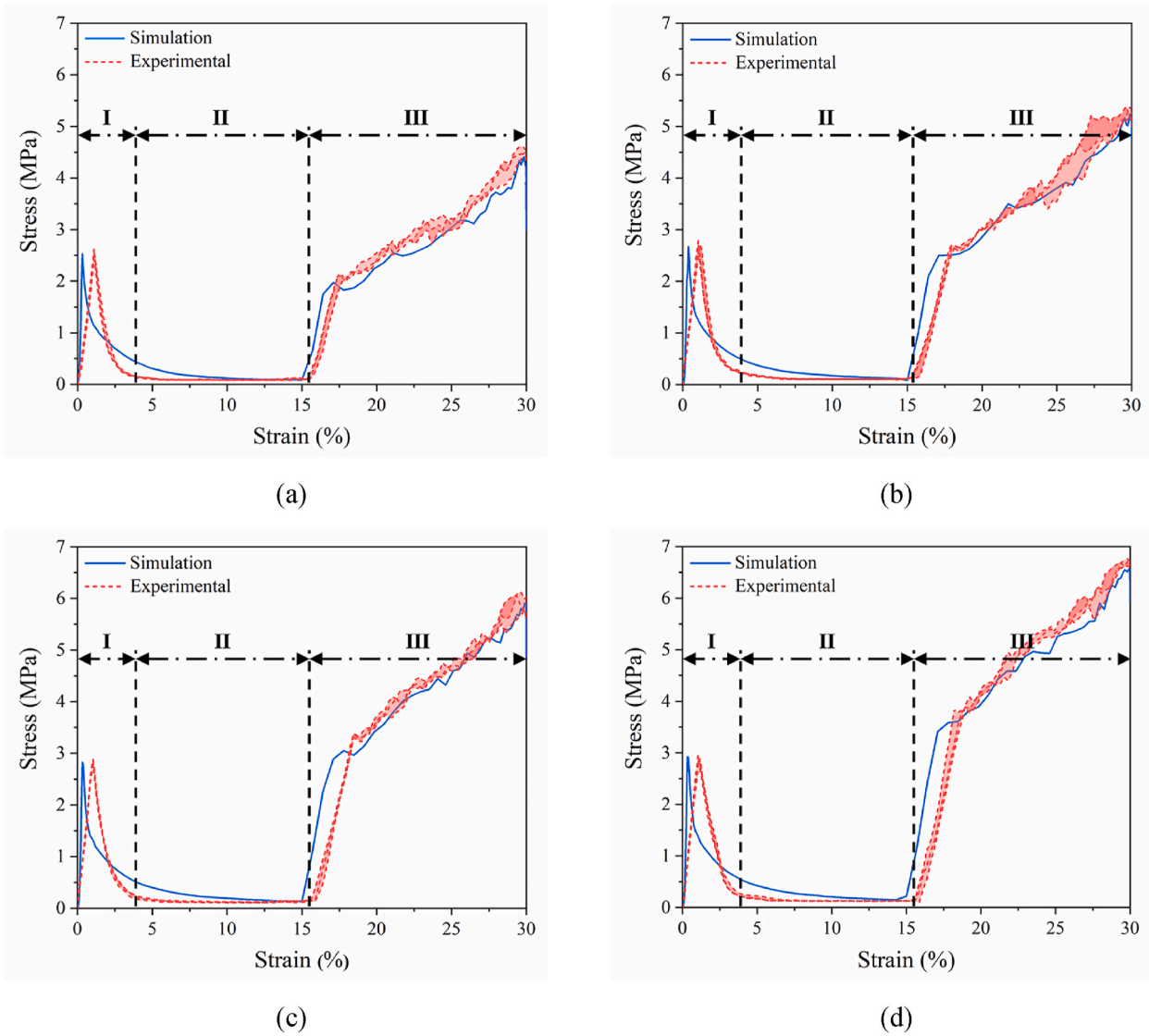

Fig. 27. Comparison of the stress–strain relationships of unit cell with various deformability under quasi-static compression between experiments and simulations: (a) P1.2; (b) P1.6; (a) P1.8; (a) P2.0.

efficiency of specimens made of strain-softening constituent materials decreases with increasing deformability or fracture energy of the constituent material. This finding aligns with the observation in section 3.1.3 that higher deformability or fracture energy in strain-softening materials promotes strain localization and disrupts the synergistic rotation of sections, leading to a loss of auxetic behavior in the unit cell.

Fig. 24 shows the ratio of energy absorption between the unit cell and the constituent material, which is another measure of energy absorption efficiency. It is defined to reflect the role of the structure in energy absorption. The energy absorption ratio decreases significantly with the increase of the deformability or the fracture energy of the constituent material, and approaches 2 in the end. This shows that although the energy absorption gradually changes from structural energy absorption to material energy absorption with increasing deformability or fracture energy of the constituent material, the energy absorption cannot be improved merely by improving the performance of the constituent materials. The asymptotic trend indicates a limit to the structural amplification effect, beyond which enhancing material properties yields diminishing returns.

When the same deformability is considered, the unit cell made of the three ductile constituent materials possesses a similar energy absorption ratio. When the deformability is smaller than 4 %, the unit cell consisting of strain-hardening material has the lowest energy absorption ratio, likely because its high strength limits the structural deformation at low ductility levels, while the opposite trend is found when deformability increases. A similar trend is observed when the same fracture energy is considered. The turning point is at 200 kJ/m^3. With the fracture energy of the constituent material increasing, the energy absorption ratio of the strain-softening material exhibits the most significant decrease. This indicates that, when high deformability or fracture energy is required for the constituent

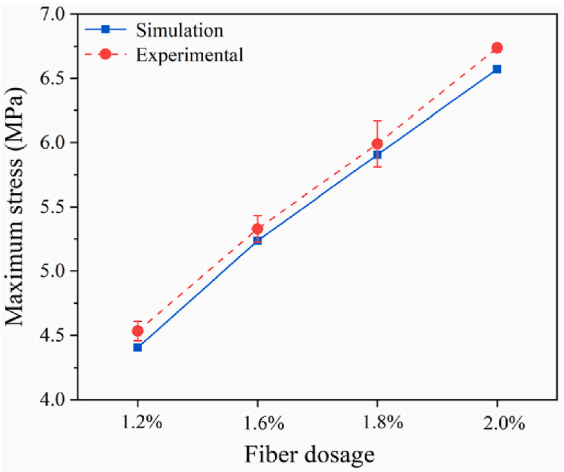

Fig. 28. Comparison of the maximum stress of unit cell with various deformability under quasi-static compression between experiments and simulations.

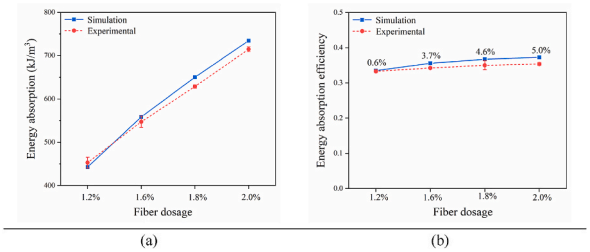

Fig. 29. Comparison of the (a) energy absorption and (b) energy absorption efficiency of unit cell with various deformability under quasi-static compression between experiments and simulations.

material, the strain-hardening material is more favorable. It can be concluded that when the deformability of the constituent material is greater than 4 % and the fracture energy of the constituent is greater than 300 kJ/m^3, the unit cell specimens made of strain-hardening constituent materials exhibit the highest energy absorption due to their optimal balance of strength and ductility.

3.1.6. Model validation

The FEM was validated by comparing the specimen deformation, stress-strain relationships, and energy absorption characteristics from the simulation with those obtained from experiments. The compression process (Fig. 25) can also be divided into three stages, which aligns with the compression process in Fig. 15. In the first stage, the peak stress in the numerical model is consistent with the experimental results, but the strain corresponding to the peak stress is different. Specifically, the stress reached the first peak when the strain reached 0.4 % in the numerical results, while the stress reached the first peak when the strain reached 1 % in the experimental results. This may be due to the elliptical hole in the middle of the cellular structure, causing a reduction in the elastic modulus of the specimen [75]. As shown in Fig. 26, the high local strain region of the unit cell at 5 % compressive strain is nearly identical to the crack region observed experimentally in Fig. 26 (b), demonstrating the model's capability to accurately predict the failure initiation locations and deformation modes. In the second stage, the level of plateau stress in simulation results (blue curves in Fig. 27) compares well with the experimental results (red curves in Fig. 27). In the third stage, the simulated stress-strain relationships agree well with experimental observations. The maximum stress of the unit cell (Fig. 28) increases with the deformability of constituent materials, consistent with the results for specimens composed of strain-hardening materials in Fig. 20 (a). For the four specimens with different deformability, the compression process in the numerical simulation matches the experimental results. The overall trends and general characteristics of the stress-strain curves are similar.

Fig. 29 compares the energy absorption characteristics of unit cells with various deformability under quasi-static compression, as obtained from experiments and simulations. The energy absorption capacity and efficiency increase with the deformability of the constituent material. The gap in energy absorption efficiency between simulation and experiments is within 5 %, indicating excellent agreement for such cellular structures and falling within acceptable engineering tolerances. In conclusion, the numerical model can accurately reproduce the deformation process, stress-strain relationships, and energy absorption characteristics of unit cells. The validated model, therefore, provides a reliable predictive tool for the behavior of cellular structures.

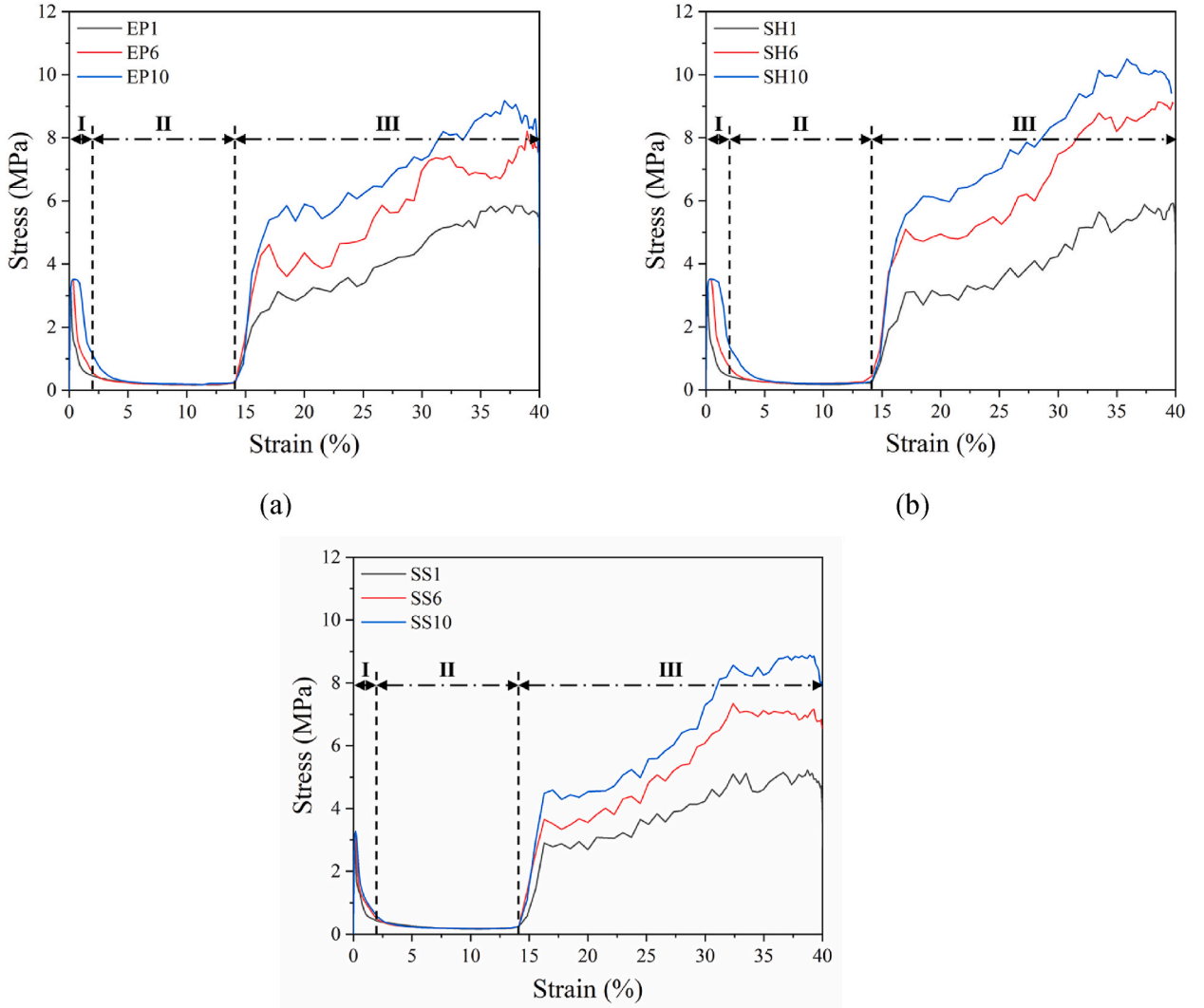

Fig. 30. Stress-strain curves of cellular cell specimens made of (a) ideal elastic-plastic, (b) strain-hardening, and (c) strain-softening constituent materials with various deformability.

3.2. Cellular structure

3.2.1. Fracture behavior

To validate the predictions of the single unit cell model, the compressive response of the 4 × 4 cellular structure was simulated and compared with the trends in Section 3.1. The simulated stress-strain curves are plotted in Figs. 30 and 31. Similar to a single cell, the compression process of all cellular structure specimens includes a rapidly increasing elastic stage, a plateau stage under low stress level, and a compaction stage where the stress increases rapidly with vertical compression. This characteristic deformation behavior has been verified experimentally [37]. The influence of the constituent materials on the stress-strain response of the cellular structure follows the same trend as that of the unit cell. Fig. 32 shows the deformation process of the cellular structure during compression (until 40 % strain). The green parts represent areas of high strain. The deformation behavior of the cellular structure can be regarded as the accumulation of deformation of each unit cell inside it.

3.2.2. Auxetic behavior, maximum load bearing capacity, energy absorption capacity and efficiency

Figs. 33 and 34 show the influence of constituent materials on critical strain (i.e., the strain at which the Poisson's ratio recovers from negative to zero), maximum load-bearing capacity, energy absorption capacity, and energy absorption efficiency of the cellular structures. The trends are consistent with those of the single unit cell shown in Section 3.1. It should be noted that, due to the

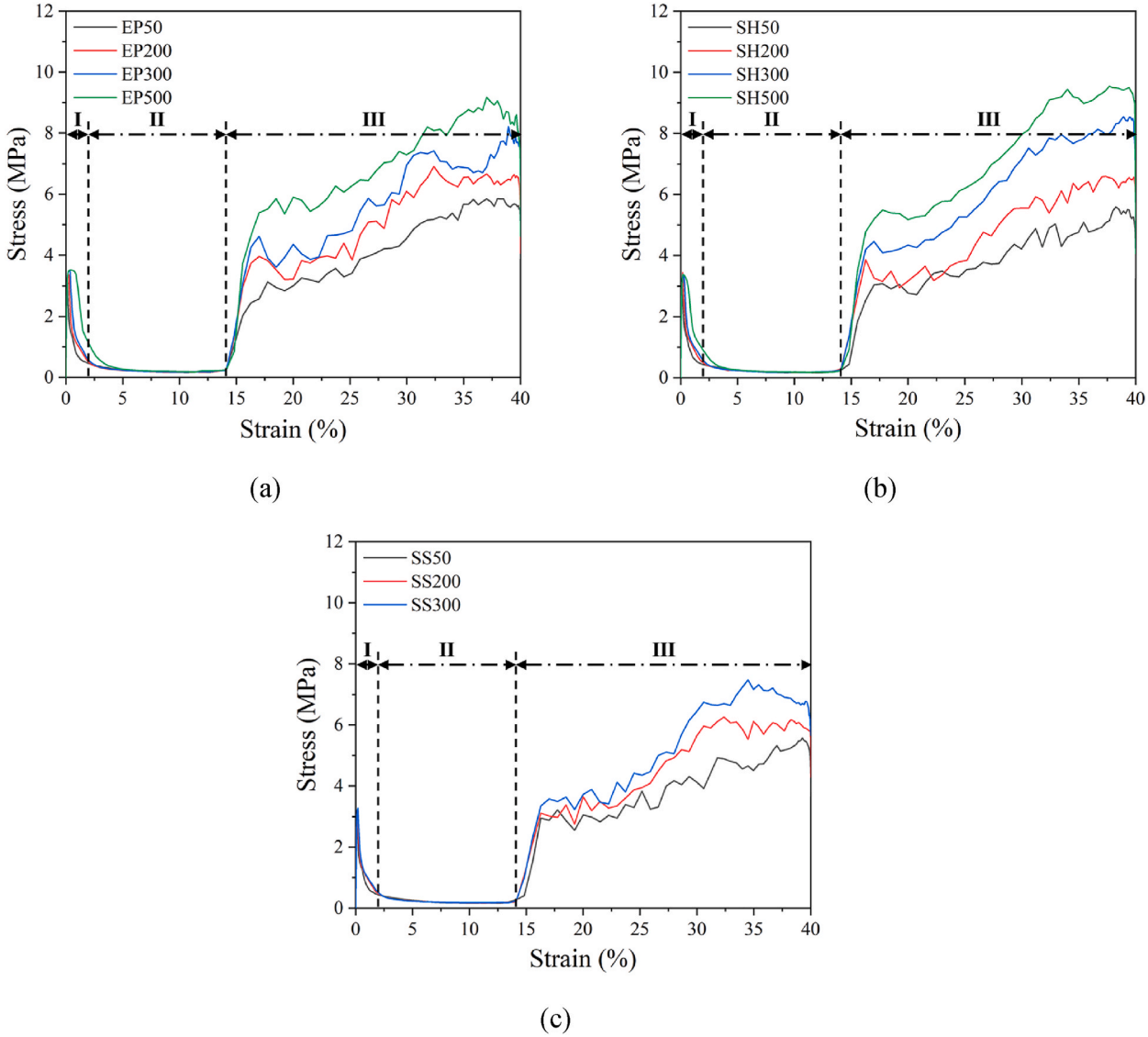

Fig. 31. Stress-strain curves of cellular cell specimens made of (a) ideal elastic-plastic, (b) strain-hardening, and (c) strain-softening constituent materials with various fracture energy.

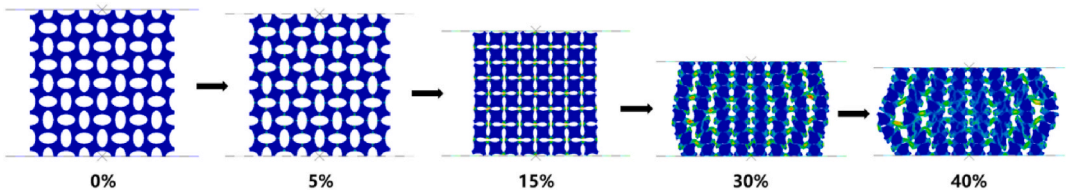

Fig. 32. Compression process of cellular structure (until 40 % strain).

accumulation of unit cell deformation, the critical strain of cellular structures made of strain-softening materials decreases more rapidly with an increase in the deformability or fracture energy of the constituent material. The proposal from Section 3.1 remains valid: strain-hardening constituent materials lead to the highest energy absorption capacity and efficiency when the deformability of the constitutive is greater than 4 % or the fracture energy exceeds 300 kJ/m^3. In cellular structures, the ratio of energy absorption between the structure and the constituent material is larger than that in the unit cell as the cells work synergistically with each other. Nevertheless, the trend of significant decline with increasing deformability or fracture energy is consistent across both scales. For the

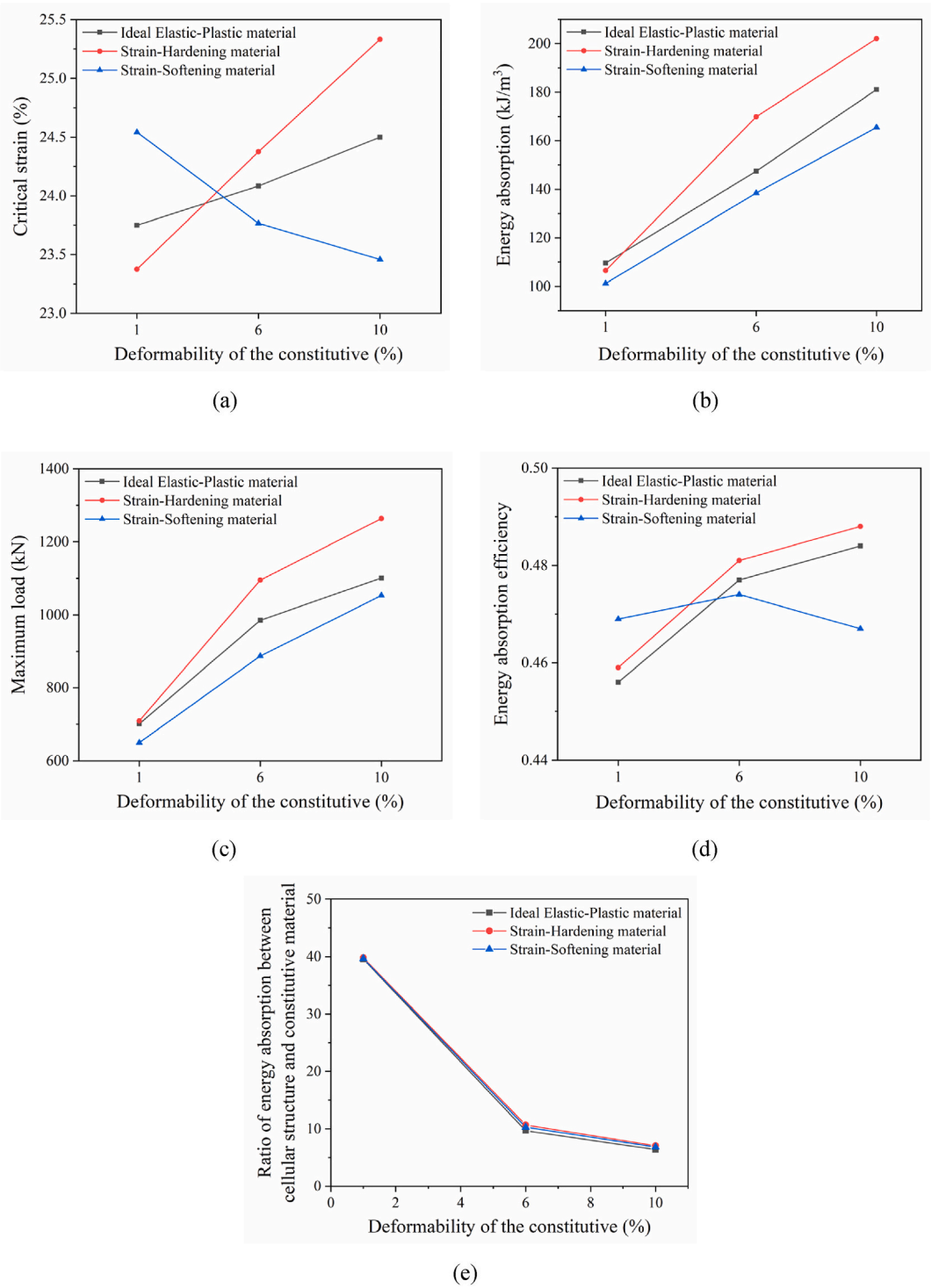

Fig. 33. Influence of deformability of constituent material on (a) the critical strain, (b) energy absorption, (c) maximum load, (d) energy absorption efficiency, and (e) ratio of energy absorption between structure and constituent material of the cellular structure.

cellular structure, the ratio ultimately approaches a value of 5. Therefore, the consistent trends observed between the cellular structure and the unit cell confirm that the single unit cell model is a reliable and efficient proxy for studying the macroscopic behavior of this auxetic cellular composite, particularly for the parametric analysis of constituent material properties.

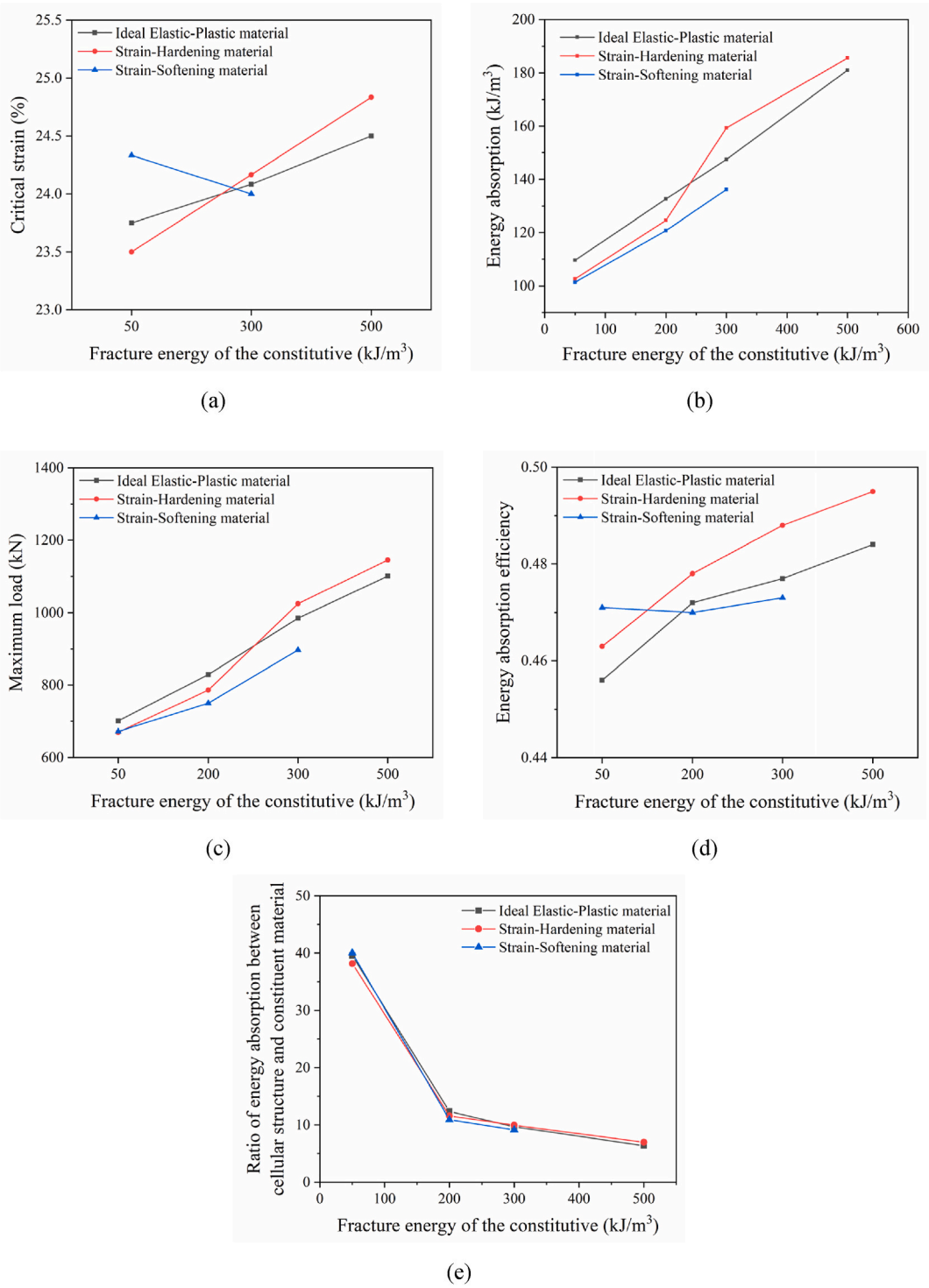

Fig. 34. Influence of fracture energy of constituent material on (a) the critical strain, (b) energy absorption, (c) maximum load, (d) energy absorption efficiency, and (e) ratio of energy absorption between structure and constituent material of the cellular structure.

4. Conclusions

The influence of the constituent material on the mechanical performance of a selected auxetic unit cell was systematically investigated using a rigorously validated numerical model. The accuracy of the unit cell model was confirmed through two

complementary validation strategies: direct experimental validation and cross-validation with a larger 4 × 4 cellular structure model. This comprehensive validation approach ensures that the simplified unit cell model reliably captures the key mechanical responses of the overall structure, thereby justifying its application in parametric studies. Based on this validated model, the following conclusions can be drawn.

- A unit cell made of an elastic-brittle constituent material does not exhibit auxetic behavior, even if the constituent material has a high elastic deformation capacity. Therefore, elastic-brittle materials should not be considered for designing auxetic cellular structures.
- Under uniaxial compression, Poisson's ratio of the cell first decreases to −1 and then increases to a positive value. The initial rate of decrease is more pronounced for the constituent materials with lower deformability or fracture energy. The strain at which Poisson's ratio reaches its minimum is independent of the constituent material considered. For ideal elastic-plastic and strain-hardening materials, increasing deformability or fracture energy leads to a larger critical strain (at which the Poisson's ratio recovers from negative to zero under compression) and also increased energy absorption efficiency. In contrast, for strain-softening materials, the opposite trends are observed for both the critical strain and energy absorption efficiency.
- The energy absorption capacity of the unit cell increases with the deformability or fracture energy of the constituent material. However, the rate of increase varies. Specifically, the energy absorption capacity increases most significantly for unit cells made of strain-hardening constituent materials and least significantly for those made of strain-softening constituent materials. There is a linear relationship between the maximum load and energy absorption capacity. This indicates that, regardless of the material's constitutive model, a higher load-bearing capacity in the compression failure stage always corresponds to a higher energy absorption ability.
- For constituent materials with low deformability or fracture energy, a strain-softening constitutive relationship may yield the highest energy absorption capacity and efficiency for the cellular structure. As the deformability and fracture energy of the constituent material increase, the strain-hardening behavior becomes superior to the strain-softening behavior in terms of energy absorption.
- The validated numerical model is able to reproduce the deformation processes, stress-strain responses, and energy absorption characteristics of unit cells and can be used to predict the behavior of the cellular structure. The influence of constituent materials on the critical strain, energy absorption, maximum load-bearing capacity, and energy absorption efficiency of the cellular structure is consistent with the trends predicted by the unit cell model. This consistency, coupled with the observation that the global deformation is essentially an accumulation of individual unit cell deformations, validates the representative nature of the unit cell model.
- With increasing deformability or the fracture energy of the constituent material, the ratio of the energy absorption of the structure to that of its constituent material decreases significantly, approaching a value of 2 for the unit cell and 5 for the cellular structure. This indicates that merely enhancing the performance of the constituent material does not necessarily improve the energy absorption of cellular composites, underscoring that optimal design requires a synergistic balance between the material and the structure, rather than a sole focus on maximizing material properties.

This study developed a replicable numerical modeling framework to investigate the influence of constituent material properties on the compressive response, auxetic behavior, and energy absorption of auxetic cellular composites. The findings, though derived from a specific geometric configuration, provide fundamental mechanistic insights. Further research incorporating different auxetic structures—such as re-entrant, chiral, or rotating units—is required to evaluate the generalizability of the proposed material-design principles. Future work will extend this framework to additional geometric configurations to further validate and generalize these findings.

CRediT authorship contribution statement

Hongzhi Zhang: Writing – review & editing, Resources, Project administration, Methodology, Funding acquisition, Conceptualization. **Shuai Song:** Writing – review & editing, Writing – original draft, Visualization, Software, Formal analysis, Data curation. **Nengdong Jiang:** Investigation, Formal analysis. **Yujie Feng:** Investigation, Formal analysis. **Jin Qin:** Software, Data curation. **Zhi Ge:** Writing – review & editing, Supervision, Resources, Project administration, Funding acquisition. **Branko Šavija:** Supervision.

Declaration of competing interest

The authors declare that they have no known competing financial interests or personal relationships that could have appeared to influence the work reported in this paper.

Acknowledgements

This work was supported by 111 Project (No. B21012), National Natural Science Foundation of China (No. 52378250), Taishan Scholars Foundation of Shandong Province (No. tsqn201909032).

Data availability

Data will be made available on request.

References

[1] R. Critchley, I. Corni, J.A. Wharton, F.C. Walsh, R.J.K. Wood, K.R. Stokes, A review of the manufacture, mechanical properties and potential applications of auxetic foams, Phys. Status Solidi 250 (10) (2023) 1963–1982, https://doi.org/10.1002/pssb.201248550.

[2] Y. Prawoto, Seeing auxetic materials from the mechanics point of view: a structural review on the negative Poisson's ratio, Comput. Mater. Sci. 58 (2012) 140–153, https://doi.org/10.1016/j.commatsci.2012.02.012.

[3] K. Li, Z. Li, Y. Wang, M.M.P. Ho, H. Hu, Low-velocity impact responses of a high-stiffness CFRP 3D hybrid auxetic lattice structure with superior energy absorption, Compos. Struct. (2025) 119604, https://doi.org/10.1016/j.compstruct.2025.119604.

[4] F. Hassani, Z. Javanbakht, S. Malek, Large deformation behavior and energy absorption of rotating square auxetics, Compos. B Eng. 283 (2024) 111596, https://doi.org/10.1016/j.compositesb.2024.111596.

[5] Q. Zhang, X. Yu, Y. Xia, D. Zhang, R.S. Lakes, K.W. Wojciechowski, F. Scarpa, The shear performance of uniaxially thermoformed auxetic polymer foams, Compos. B Eng. 286 (2024) 111791, https://doi.org/10.1016/j.compositesb.2024.111791.

[6] J. Ju, J.D. Summers, Compliant hexagonal periodic lattice structures having both high shear strength and high shear strain, Mater. Des. 32 (2) (2011) 512–524, https://doi.org/10.1016/j.matdes.2010.08.029.

[7] T. Li, F. Liu, L. Wang, Enhancing indentation and impact resistance in auxetic composite materials, Compos. B Eng. 198 (2020) 108229, https://doi.org/10.1016/j.compositesb.2020.108229.

[8] L.L. Hu, M.Z. Zhou, H. Deng, Dynamic indentation of auxetic and non-auxetic honeycombs under large deformation, Compos. Struct. 207 (2019) 323–330, https://doi.org/10.1016/j.compstruct.2018.09.066.

[9] D. Shi, Z. Wang, Y. Li, R. Huo, J. Zhang, J. Cai, A novel re-entrant circular star-shaped auxetic honeycomb with enhanced energy absorption and anisotropic poisson's ratio, Mater. Des. 257 (2025) 114465, https://doi.org/10.1016/j.matdes.2025.114465.

[10] A.N. Biswas, N. Mahesh, S.R. Peri, B.R. Krishnan, P.R. Sreekanth, Hybrid auxetic materials implemented in crates & non-pneumatic wheels for shock absorption, Mater. Today Proc. 56 (2022) 1327–1334, https://doi.org/10.1016/j.matpr.2021.11.326.

[11] K.E. Evans, A. Alderson, Auxetic materials: functional materials and structures from lateral thinking, Adv. Mater. 12 (9) (2000) 617–628, https://doi.org/10.1002/(SICI)1521-4095(200005)12:9<617::AID-ADMA617>3.0.CO;2-3.

[12] N. Karnessis, G. Burriesci, Uniaxial and buckling mechanical response of auxetic cellular tubes, Smart Mater. Struct. 22 (8) (2013) 084008, https://doi.org/10.1088/0964-1726/22/8/084008.

[13] R.H. Baughman, J.M. Shacklette, A.A. Zakhidov, S. Stafström, Negative Poisson's ratios as a common feature of cubic metals, Nature 392 (6674) (1998) 362–365.

[14] H. Qin, Y. Sun, J.Z. Liu, M. Li, Y. Liu, Negative Poisson's ratio in rippled graphene, Nanoscale 9 (12) (2017) 4135–4142, https://doi.org/10.1039/C6NR07911C.

[15] C. Sanchez-Valle, Z.A. Lethbridge, S.V. Sinogeikin, J.J. Williams, R.I. Walton, K.E. Evans, et al., Negative Poisson's ratios in siliceous zeolite MFI-silicalite, J. Chem. Phys. 128 (18) (2008) 184503, https://doi.org/10.1063/1.2912061.

[16] N.R. Keskar, J.R. Chelikowsky, Negative Poisson ratios in crystalline SiO_2 from first-principles calculations, Nature 358 (6383) (1992) 222–224.

[17] J.L. Williams, J.L. Lewis, Properties and an anisotropic model of cancellous bone from the proximal tibial epiphysis, J. Biomech. Eng. 104 (1) (1982) 50–56, https://doi.org/10.1115/1.3138303.

[18] C. Lees, J.F. Vincent, J.E. Hillerton, Poisson's ratio in skin, Bio Med. Mater. Eng. 1 (1) (1991) 19–23.

[19] N. Wang, Auxetic nuclei, Nat. Mater. 13 (6) (2014) 540–542.

[20] T. Yamamoto, H. Schiessel, Chromatin gels are auxetic due to cooperative nucleosome assembly and disassembly dynamics, EPL 118 (2) (2017), https://doi.org/10.1209/0295-5075/118/28003.

[21] H.C. Luo, X. Ren, Y. Zhang, X.Y. Zhang, X.G. Zhang, C. Luo, X. Cheng, Y.M. Xie, Mechanical properties of foam-filled hexagonal and re-entrant honeycombs under uniaxial compression, Compos. Struct. 280 (2022) 114922, https://doi.org/10.1016/j.compstruct.2021.114922.

[22] R. Zhong, X. Ren, X.Y. Zhang, C. Luo, Y. Zhang, Y.M. Xie, Mechanical properties of concrete composites with auxetic single and layered honeycomb structures, Constr. Build. Mater. 322 (2022) 126453, https://doi.org/10.1016/j.conbuildmat.2022.126453.

[23] X. Zhang, X. Shan, G. Sui, C. Hou, X. Du, Z. Min, T. Xie, Enhancing piezoelectric energy harvesters with rotating triangular auxetic structures, Int. J. Mech. Sci. 289 (2025) 110081, https://doi.org/10.1016/j.ijmecsci.2025.110081.

[24] P. Wang, X. Ren, J. Zhang, P. Zhu, J. Kang, J. Zhou, Z. Cheng, H. Feng, Advanced 3D-Printed auxetic structures: mechanical performance evaluation of ECC in rotating rigid configurations, Cement Concr. Compos. 161 (2025) 106101, https://doi.org/10.1016/j.cemconcomp.2025.106101.

[25] C.S. Ha, M.E. Plesha, R.S. Lakes, Chiral three-dimensional lattices with tunable Poisso's ratio, Smart Mater. Struct. 25 (2016) 054005, https://doi.org/10.1088/0964-1726/25/5/054005.

[26] Y. Zhang, X. Ren, W. Jiang, D. Han, X.Y. Zhang, Y. Pan, Y.M. Xie, In-plane compressive properties of assembled auxetic chiral honeycomb composed of slotted wave plate, Mater. Des. 221 (2022) 110956, https://doi.org/10.1016/j.matdes.2022.110956.

[27] X.G. Zhang, X. Ren, W. Jiang, X.Y. Zhang, C. Luo, Y. Zhang, Y.M. Xie, A novel auxetic chiral lattice composite: experimental and numerical study, Compos. Struct. 282 (2022) 115043, https://doi.org/10.1016/j.compstruct.2021.115043.

[28] J. Yang, S. Zhao, J. Yang, Recent advances in graphene origami-enabled auxetic metamaterial structures, Eng. Struct. 333 (2025) 120203, https://doi.org/10.1016/j.engstruct.2025.120203.

[29] J. Pitchaimani, S. Kattimani, Non-linear thermal stability and free vibration behavior of sandwich beams with auxetic re-entrant aluminum cores and graphene origami-enhanced facings, Compos. Struct. (2025) 119564, https://doi.org/10.1016/j.compstruct.2025.119564.

[30] Q. Gao, W.H. Liao, C. Huang, Theoretical predictions of dynamic responses of cylindrical sandwich filled with auxetic structures under impact loading, Aero. Sci. Technol. 107 (2020) 106270, https://doi.org/10.1016/j.ast.2020.106270.

[31] Q. Gao, W.H. Liao, Energy absorption of thin walled tube filled with gradient auxetic structures-theory and simulation, Int. J. Mech. Sci. 201 (2021) 106475, https://doi.org/10.1016/j.ijmecsci.2021.106475.

[32] M.J. Mirzaali, R. Hedayati, P. Vena, L. Vergani, M. Strano, A.A. Zadpoor, Rational design of soft mechanical metamaterials: independent tailoring of elastic properties with randomness, Appl. Phys. Lett. 111 (5) (2017), https://doi.org/10.1063/1.4989441.

[33] H.L. Tan, Z.C. He, K.X. Li, E. Li, A.G. Cheng, B. Xu, In-plane crashworthiness of re-entrant hierarchical honeycombs with negative Poisson's ratio, Compos. Struct. 229 (2019) 111415, https://doi.org/10.1016/j.compstruct.2019.111415.

[34] H.M.A. Kolken, A.F. Garcia, A. Plessis Du, C. Rans, M.J. Mirzaali, A.A. Zadpoor, Fatigue performance of auxetic meta-biomaterials, Acta Biomater. 126 (2021) 511–523, https://doi.org/10.1016/j.actbio.2021.03.015.

[35] I.G. Masters, K.E. Evans, Models for the elastic deformation of honeycombs, Compos. Struct. 35 (1996) 403–422, https://doi.org/10.1016/S0263-8223(96)00054-2.

[36] Y. Xu, E. Schlangen, M. Luković, B. Šavija, Tunable mechanical behavior of auxetic cementitious cellular composites (CCCs): experiments and simulations, Constr. Build. Mater. 266 (2021) 121388, https://doi.org/10.1016/j.conbuildmat.2020.121388.

[37] Y. Xu, H. Zhang, E. Schlangen, M. Luković, B. Šavija, Cementitious cellular composites with auxetic behavior, Cement Concr. Compos. 111 (2020) 103624, https://doi.org/10.1016/j.cemconcomp.2020.103624.

[38] I.E. Berinskii, Elastic networks to model auxetic properties of cellular materials, Int. J. Mech. Sci. 115–116 (2016) 481–488, https://doi.org/10.1016/j.ijmecsci.2016.07.038.

[39] G.A. Lyngdoh, N.-K. Kelter, S. Doner, N.M.A. Krishnan, S. Das, Elucidating the auxetic behavior of cementitious cellular composites using finite element analysis and interpretable machine learning, Mater. Des. 213 (2022) 110341, https://doi.org/10.1016/j.matdes.2021.110341.

[40] D.A. White, J. Kudo, K. Swartz, D.A. Tortorelli, S. Watts, A reduced order model approach for finite element analysis of cellular structures, Finite Elem. Anal. Des. 214 (2023) 103855, https://doi.org/10.1016/j.finel.2022.103855.

[41] T. Li, J. Sun, J. Leng, Y. Liu, Quasi-static compressive behavior and energy absorption of novel cellular structures with varying cross-section dimension, Compos. Struct. 306 (2023) 116582, https://doi.org/10.1016/j.compstruct.2022.116582.

[42] X. Shuang, D. Qingtian, L. Xinbo, Z. Jiabao, W. Jinpeng, Y. Zhirong, Energy absorption and deformation of cellular structures with dovetail joints, Mech. Res. Commun. 143 (2025) 104353, https://doi.org/10.1016/j.mechrescom.2024.104353.

[43] D. Han, X. Ren, Y. Zhang, X. Zhang, X. Zhang, C. Luo, et al., Lightweight auxetic metamaterials: design and characteristic study, Compos. Struct. 293 (2022) 115706, https://doi.org/10.1016/j.compstruct.2022.115706.

[44] B. Taherkhani, M.B. Azizkhani, J. Kadkhodapour, A.P. Anaraki, S. Rastgordani, Highly sensitive, piezoresistive, silicone/carbon fiber-based auxetic sensor for low strain values, Sensor Actuator Phys. 305 (2020) 111939, https://doi.org/10.1016/j.sna.2020.111939.

[45] L. Valentini, S. Bittolo Bon, N.M. Pugno, Graphene and carbon nanotube auxetic rubber bionic composites with negative variation of the electrical resistance and comparison with their nonbionic counterparts, Adv. Funct. Mater. 27 (24) (2017) 1606526, https://doi.org/10.1002/adfm.201606526.

[46] X., J. Shen, A. Ghaedizadeh, H. Tian, Y.M. Xie, Experiments and parametric studies on 3D metallic auxetic metamaterials with tuneable mechanical properties, Smart Mater. Struct. 24 (9) (2015) 095016, https://doi.org/10.1088/0964-1726/24/9/095016.

[47] R. Hedayati, M. Sadighi, M. Mohammadi-Aghdam, A. Zadpoor, Mechanical properties of additively manufactured octagonal honeycombs, Mater. Sci. Eng. C 69 (2016) 1307–1317, https://doi.org/10.1016/j.msec.2016.08.020.

[48] R. Hamzehei, J. Kadkhodapour, A.P. Anaraki, S. Rezaei, S. Dariushi, A.M. Rezadoust, Octagonal auxetic metamaterials with hyperelastic properties for large compressive deformation, Int. J. Mech. Sci. 145 (2018) 96–105, https://doi.org/10.1016/j.ijmecsci.2018.06.040.

[49] J. Zhang, G. Lu, Z. You, Large deformation and energy absorption of additively manufactured auxetic materials and structures: a review, Composites, Part B 201 (2020) 108340, https://doi.org/10.1016/j.compositesb.2020.108340.

[50] C. Yang, H.D. Vora, Y. Chang, Behavior of auxetic structures under compression and impact forces, Smart Mater. Struct. 27 (2) (2018) 025012, https://doi.org/10.1088/1361-665X/aaa3cf.

[51] T. Fíla, P. Zlámal, O. Jiroušek, J. Falta, P. Koudelka, D. Kytýř, et al., Impact testing of polymer-filled auxetics using split hopkinson pressure bar, Adv. Eng. Mater. 19 (10) (2017) 1700076, https://doi.org/10.1002/adem.201700076.

[52] J. Xie, S. He, Y. Xu, Z. Meng, W. Zhou, E. Schlangen, B. Šavija, Enhanced elastomer-like auxetic cementitious materials through strain-hardening cementitious composites (SHCC) with extended softening properties, Cement Concr. Compos. 161 (2025) 106069, https://doi.org/10.1016/j.cemconcomp.2025.106069.

[53] M. Kucewicz, P. Baranowski, J. Małachowski, A method of failure modeling for 3D printed cellular structures, Mater. Des. 174 (2019) 107802, https://doi.org/10.1016/j.matdes.2019.107802.

[54] X. Zhang, X. Ren, A simple methodology to generate metamaterials and structures with negative poisson's ratio, Phys. Status Solidi 257 (10) (2020) 2000439, https://doi.org/10.1002/pssb.202000439.

[55] Y. Chi, M. Yu, L. Huang, L. Xu, Finite element modeling of steel-polypropylene hybrid fiber reinforced concrete using modified concrete damaged plasticity, Eng. Struct. 148 (2017) 23–35, https://doi.org/10.1016/j.engstruct.2017.06.039.

[56] V.V. Saykin, T.H. Nguyen, J.F. Hajjar, D. Deniz, J. Song, Material characterization using finite element deletion strategies for collapse modeling of steel structures, Eng. Struct. 147 (2017) 125–133, https://doi.org/10.1016/j.engstruct.2017.05.059.

[57] H. Ranganathan, D. André, M. Mouiya, M. Huger, R. Soth, C. Wöhrmeyer, A multiscale discrete element thermomechanical modeling approach of microcracking generated at high temperature by anisotropic thermal expansion in an elastic brittle polycrystalline ceramic material, Eng. Fract. Mech. 320 (2025) 111088, https://doi.org/10.1016/j.engfracmech.2025.111088.

[58] L. Liu, K. Shinozaki, Brittle–ductile transition and toughening of silica glass via Ni nanoparticle incorporation at a small volume fraction, J. Alloys Compd. 940 (2023) 168874, https://doi.org/10.1016/j.jallcom.2023.168874.

[59] Z. Kovács, L.S. Tóth, J. Lendvai, Ideal elasto-plastic behavior in torsional deformation of $Zr_{44}Ti_{11}Cu_{10}Ni_{10}Be_{25}$ bulk metallic glass, J. Alloys Compd. 542 (2012) 85–89, https://doi.org/10.1016/j.jallcom.2012.07.058.

[60] P. Yu, H. Yang, Z. Ren, Z. Chen, T. Li, A multi-scale modeling method for tensile properties of strain-hardening cementitious composites, J. Build. Eng. 97 (2024) 110924, https://doi.org/10.1016/j.jobe.2024.110924.

[61] J. Pan, Y.P. Ivanov, W.H. Zhou, Y. Li, A.L. Greer, Strain-hardening and suppression of shear-banding in rejuvenated bulk metallic glass, Nature 578 (7796) (2020) 559–562, https://doi.org/10.1038/s41586-020-2016-3.

[62] X. Li, W.G. Cao, Y.H. Su, A statistical damage constitutive model for softening behavior of rocks, Eng. Geol. 143 (2012) 1–17, https://doi.org/10.1016/j.enggeo.2012.05.005.

[63] W. Sae-Long, N. Damrongwiriyanupap, S. Limkatanyu, Y. Xi, P. Sukontasukkul, T. Phoo-Ngernkham, C. Buachart, A two-step composite mechanics approach for post-peak behavior of concrete incorporating both natural and recycled concrete aggregates, Constr. Build. Mater. 490 (2025) 142365, https://doi.org/10.1016/j.conbuildmat.2025.142365.

[64] C. An, M. Duan, R.D. Toledo Filho, S.F. Estefen, Collapse of sandwich pipes with PVA fiber reinforced cementitious composites core under external pressure, Ocean Eng 82 (2014) 1–13, https://doi.org/10.1016/j.oceaneng.2014.02.023.

[65] J. Wang, X. Yu, Y. Fu, G. Zhou, A 3D meso-scale model and numerical uniaxial compression tests on concrete with the consideration of the friction effect, Materials 17 (5) (2024) 1204, https://doi.org/10.3390/ma17051204.

[66] Recommendations for Design and Construction of High-Performance Fiber Reinforced Cement Composites with Multiple Fine Cracks, Japan Society of Civil Engineers, Tokyo, Japan, 2008, pp. 1–16.

[67] M. Taylor, L. Francesconi, A. Baldi, X. Liang, F. Aymerich, A novel auxetic structure with enhanced impact performance by means of periodic tessellation with variable poisson's ratio, in: J. Kimberley, L. Lamberson, S. Mates (Eds.), Dynamic Behavior of Materials, Conference Proceedings of the Society for Experimental Mechanics Series, 1, Springer, Cham, 2019, pp. 211–218, https://doi.org/10.1007/978-3-319-95089-1_38.

[68] J.X. Qiao, C.Q. Chen, Impact resistance of uniform and functionally graded auxetic double arrowhead honeycombs, Int. J. Impact Eng. 83 (2015) 47–58, https://doi.org/10.1016/j.ijimpeng.2015.04.005.

[69] M.F. Ashby, R.F.M. Medalist, The mechanical properties of cellular solids, Metall. Trans. A 14 (9) (1983) 1755–1769.

[70] L. Zhang, S. Feih, S. Daynes, S. Chang, M.Y. Wang, J. Wei, et al., Energy absorption characteristics of metallic triply periodic minimal surface sheet structures under compressive loading, Addit. Manuf. 23 (2018) 505–515, https://doi.org/10.1016/j.addma.2018.08.007.

[71] C. Garrido, G. Pincheira, R. Valle, J. Fernández, V. Tuninetti, Plastic deformation behavior and energy absorption performance of a composite metamaterial based on asymmetric auxetic lattices, Compos. Struct. 346 (2024) 118410, https://doi.org/10.1016/j.compstruct.2024.118410.

[72] J.G. Eom, Y.H. Son, S.W. Jeong, S.T. Ahn, S.M. Jang, D.J. Yoon, M.S. Joun, Effect of strain hardening capability on plastic deformation behaviors of material during metal forming, Mater. Des. 54 (2014) 1010–1018, https://doi.org/10.1016/j.matdes.2013.08.101.

[73] J. Miltz, G. Gruenbaum, Evaluation of cushioning properties of plastic foams from compressive measurements, Polym. Eng. Sci. 21 (15) (1981) 1010–1014, https://doi.org/10.1002/pen.760211505.

[74] B. Xie, Y.Z. Fan, T.Z. Mu, B. Deng, Fabrication and energy absorption properties of titanium foam with $CaCl_2$ as a space holder, Materials Science and Engineering: A 708 (2017) 419–423, https://doi.org/10.1016/j.msea.2017.09.123.

[75] J. Fang, K. Yang, X. Lyu, J. Tang, J. Zhang, Mechanical properties and instability analysis of concrete specimens with horizontal holes of different diameters, Front. Earth Sci. 10 (2022) 949043, https://doi.org/10.3389/feart.2022.949043.